American Mineralogist, Volume 95, pages 1276–1293, 2010

Unique crystal chemistry of two polymorphs of topaz-OH: A multi-nuclear NMR and Raman study

Xianyu Xue,* Masami Kanzaki, and Hiroshi Fukui†

Institute for Study of the Earth's Interior, Okayama University, Misasa, Tottori, 682-0193, Japan

Abstract

A new polymorph of topaz-OH (denoted as topaz-OH II) was recently discovered at higher *P-T* conditions than has been known thus far (denoted as topaz-OH I). High-resolution ^{1}H, ^{29}Si, and ^{27}Al nuclear magnetic resonance (NMR) and micro-Raman spectroscopy are applied to shed light on the crystal chemistry of both polymorphs. Topaz-OH I, synthesized at 7 GPa and 640 °C, is stoichiometric (Si/Al = 0.5) with a largely ordered local structure. Higher *P-T* topaz-OH I synthesized at conditions close to the polymorphic phase transition boundary, on the other hand, shows lower Si/Al ratios (0.44–0.45) and greater local structural disorder [including a small fraction (~3%) of octahedral Si with a unique ^{29}Si chemical shift near –133 ppm]. The latter may be accounted for by the development of defects (Si/Al in normally vacant octahedral sites and vacancies in the tetrahedral sites) at higher *P-T* conditions. Topaz-OH II synthesized at 13.5~14 GPa and 1300~1400 °C similarly exhibits low Si/Al ratios (0.41–0.46). The NMR and Raman spectra for these topaz-OH II are, in general, broader and revealed a substantial fraction (33–37%) of octahedral Si with a range of ^{29}Si chemical shifts (–130 to –190 ppm), a small fraction (2–3%) of tetrahedral Al, and a range of (and overall shorter) hydrogen-bonding distances than topaz-OH I. Therefore, the phase transition from topaz-OH I to II is characterized by both a significant increase in the occupied octahedral/tetrahedral site ratio as well as disordering of cation distribution, which is unique from the viewpoint of crystal chemistry.

Keywords: NMR spectroscopy, Raman spectroscopy, high pressure, crystal structure, phase transition, vacancy, vacant site, Al-Si disorder, hydrogen bonding

Introduction

Naturally occurring topaz [$Al_2SiO_4(F,OH)_2$] are generally limited to F-rich compositions. Topaz-OH [$Al_2SiO_4(OH)_2$], the OH end-member of the F-OH solid-solution series of topaz, was first synthesized at 5.5–10 GPa and 700–1000 °C (Wunder et al. 1993). Subsequent studies in the Al_2O_3-SiO_2-H_2O system reported that topaz-OH can occur at pressures up to ca. 13 GPa and temperatures up to ca. 1500 °C, and breaks down to phase egg ($AlSiO_3OH$)-bearing assemblages at higher pressures and to kyanite (Al_2SiO_5) + fluid at higher temperatures (Ono 1999; Schmidt et al. 1998).

Despite the reported high-temperature stability (up to ca. 1500 °C at 13 GPa) (Ono 1999), only topaz-OH samples synthesized at relatively low *P-T* (up to 10 GPa and 1000 °C) have been well characterized. Wunder et al. (1993) first refined the crystal structure of topaz-OH synthesized at 10 GPa and 1000 °C (space group *Pbnm*) from single-crystal X-ray diffraction (XRD). Subsequent studies of topaz-OH synthesized at 10 GPa and 1000 °C by single-crystal XRD (Northrup et al. 1994) and topaz-OD synthesized at 7.5 GPa and 750 °C by powder neutron diffraction (Chen et al. 2005) located the H (D) positions, and reported that the single H position found in F-rich topaz is split into two nonequivalent, half-occupied H (D) positions in topaz-OH (OD). The reported infrared and Raman spectra for topaz-OH synthesized at 9–10 GPa and 800–1000 °C both contain two O-H stretching bands near 3600 and 3520 cm^{-1} with a low-frequency shoulder (Komatsu et al. 2005; Wunder et al. 1993). These bands have been attributed to O-H stretching of different OH groups from ab-initio calculations (Churakov and Wunder 2004).

We have applied a combined nuclear magnetic resonance (NMR) and micro-Raman spectroscopic study on hydrous phases (topaz-OH, phase egg, and δ-AlOOH) in the Al_2O_3-SiO_2-H_2O system synthesized under a range of *P-T* conditions to place additional constraints on their structures and potential roles as water reservoirs in the Earth's mantle (Kanzaki et al. 2006; Xue et al. 2006). During this study, we discovered a new polymorph of topaz-OH (denoted here as topaz-OH II) (Kanzaki et al. 2006). In-situ XRD measurements over a wide range of *P-T* using synchrotron radiation at SPring-8, Japan, revealed that topaz-OH II occurs at the highest *P-T* corner of the previously reported stability field for topaz-OH, and the phase transition between topaz-OH II and the polymorph known thus far (denoted as topaz-OH I) is reversible (Kanzaki, unpublished results). The crystal structure of topaz-OH II has recently been refined in space group *Pbnm* using powder XRD data obtained with synchrotron radiation at SPring-8, and was found to bear some resemblance to that of topaz-OH I, but with a disordered cation distribution

* E-mail: xianyu@misasa.okayama-u.ac.jp

† Present address: Department of Material Science, Graduate School of Material Science, University of Hyogo, 3-2-1, Kamigohri, Hyogo 678-1279, Japan.

(Kanzaki 2010). Here we report detailed high-resolution, multinuclear (^{1}H, ^{29}Si, ^{27}Al) NMR and Raman results on topaz-OH (I and II) synthesized at 7–14 GPa, 640–1500 °C to further shed light on the unique crystal chemistry of both polymorphs.

Experimental methods

Sample syntheses

Topaz-OH II was first encountered during preliminary experiments aimed at synthesizing phase egg at high temperatures (≥1200 °C) using a nominal bulk composition of $AlSiO_3OH$ (by H.F.) with a 1000 or 5000 ton Kawai-type double-stage uniaxial split-sphere multi-anvil apparatus (USSA-1000 or 5000) at the Institute for Study of the Earth's Interior (ISEI) (Kanzaki et al. 2006). Some of the experiments were performed using high-pressure cell assemblies that lacked accurate pressure calibration, which fortunately led to the unexpected synthesis of topaz-OH II with unusual Raman and NMR features (Kanzaki et al. 2006).

All the samples described in this paper (see Table 1) have been synthesized subsequently (by M.K.) using a Kawai-type double stage multi-anvil system with a DIA-type guide block driven by a 1500 ton press (SPEED1500) installed in the beamline BL04B1 of SPring-8. These "quench experiments" were performed either in preparation for, or as a follow-up to in situ measurements with synchrotron radiation (Kanzaki, unpublished results), and used the same cell assemblies. Pressure was estimated from the pressure-press load relationship of the corresponding in situ experiments with similar initial press load and final temperature, with estimation uncertainties <1 GPa. The starting material was a mixture of dried reagent-grade SiO_2, Al_2O_3, and $Al(OH)_3$ with a nominal bulk composition of $Al_2SiO_4(OH)_2$, and was either sealed into a 2 or 3 mm (OD) Pt capsule by welding shut or enclosed in a 1.4 mm Ag-Pd capsule without sealing (see Table 1). For all samples except K081113, a Cr-doped MgO octahedral cell assembly with an edge length of 14 mm and a BN composite tube heater (Kanzaki 2010) were used. For sample K081113, an 18 mm octahedral cell assembly and a graphite tube heater were used. Temperature was measured with a W97Re3-W75Re25 thermocouple with uncertainties within ±1 °C for most experiments, but was estimated from the heating power with estimation uncertainties within ca. ±100 °C for samples K081113 and K071126 because of the failure of the thermocouple (see Table 1). Temperature gradient across the sample (ca. 2 mm length) is expected to be within ca. 100 °C for all experiments. High-pressure experiments were carried out by initial compression to the desired pressure, followed by heating to the desired temperature. After keeping the sample at the target *P-T* condition for a duration of 0.5–3 h, it was quenched by cutting the electrical power to the heater, followed by decompression.

Electron microprobe analysis

Chemical analysis and mapping have been performed on selected pieces of each sample (embedded in epoxy and polished) using a JEOL JXA-8800 electron microprobe. An accelerating voltage of 10 kV, a beam diameter of 2 µm, a counting time of 20 s on peak, and 10 s on the background were used for the chemical analysis. To ensure both minimal damages to the sample and good statistics, test measurements were first performed on a large single crystal of topaz-OH (K080927) and the standards (quartz and corundum) using beam currents of 1, 5, and 10 nA. The average compositions (for 10 measurements each) were the same within analytical uncertainties for all, but the standard deviations are smaller with beam currents ≥5 nA. Therefore, all the final (reported) results have been obtained with a beam current of 5 nA [as compared to 1 nA in our earlier study (Xue et al. 2006)]. Ten to 25 analyses have been made for each sample (unless otherwise noted), and the average compositions are reported in Table 2.

Raman spectroscopy

Unpolarized Raman spectra were acquired using an argon-ion laser with a wavelength of 488 nm and a power of 60 mW in a 180° backscattering geometry, similar to that described previously (Xue et al. 2006). The laser beam was focused onto the sample with a 50× objective lens. Scattered light from the sample was focused onto a pinhole (diameter: 100 µm) before entering an imaging monochromater with a focal length of 500 mm and a grating of 1200 gr/mm, and detected with a liquid nitrogen-cooled CCD detector. Raman shift was calibrated using the plasma lines of the laser. The exposure time was typically 60 s.

^{1}H, ^{29}Si, and ^{27}Al NMR spectroscopy

^{1}H, ^{29}Si, and ^{27}Al MAS NMR spectra were obtained at a resonance frequency of 400.4, 79.5, and 104.3 MHz, respectively, using a Varian Unity-Inova 400 MHz spectrometer and a Varian 2.5 or 1.6 mm T3 MAS probe. Chemical shifts are referenced externally to tetramethylsilane (TMS) for ^{1}H and ^{29}Si, and to 1 *M* aqueous solution of $Al(NO_3)_3$ for ^{27}Al, and are reproducible to better than ±0.1 ppm.

^{1}H MAS NMR spectra have been obtained with a spectral width of 1 MHz, a range of sample spinning rates up to 40 kHz, and recycle delay times of 3 to 15 s [$\geq 5*T_1(^1H)$ for topaz-OH, where T_1 is the spin-lattice relaxation time constant] using a Varian 1.6 mm T3 MAS probe. The ^{1}H T_1 was measured with the saturation-recovery method, and was found to be 0.9–4.4 s for the topaz-OH polymorphs (see Table 3). The DEPTH sequence that consists of three back-to-back pulses $\pi/2$-π-π) with a phase cycle of 16 (Cory and Ritchey 1988) was used, which effectively suppressed the background to a negligible level with the 1.6 mm T3 MAS probe.

Because ^{1}H has the highest magnetogyric ratio among all naturally occurring isotopes, ^{1}H MAS NMR spectra of hydrous phases often suffer from peak broadening due to residual homonuclear dipolar coupling. The contribution to the peak width from the latter is expected to decrease linearly with decreasing $1/\nu_R$ (where ν_R is the spinning frequency), although depending on the proton concentration/distributions, it is often still significantly above the natural peak width even at a spinning rate of 40 kHz (Xue and Kanzaki 2009).

An alternative and often more effective method to achieve high resolution for ^{1}H is the family of CRAMPS (combined rotation and multiple pulse spectroscopy) techniques that utilizes multiple pulses to eliminate homonuclear dipolar coupling among protons (Xue and Kanzaki 2009). To achieve higher resolution to allow proton order/disorder directly probed, we have obtained two-dimensional (2D) ^{1}H CRAMPS-MAS NMR spectra for all samples using a Varian 1.6 mm T3 MAS NMR probe. The frequency-switched Lee-Goldburg (FSLG) scheme (Bielecki et al. 1989) was used at a spinning rate of 15 kHz for proton homonuclear decoupling. The pulse sequence is similar to that described in Xue and Kanzaki (2007): following a preparation $\pi/2$ pulse, FSLG decoupling (with an RF field of 107 kHz) was applied during the evolution time period t_1. A second $\pi/2$ pulse was then applied to rotate the magnetization back to z axis. After a minimal delay (typically 2 µs), a third $\pi/2$ pulse was applied, followed by data acquisition. For spin diffusion experiment, a longer mixing time (typically 200 ms) was inserted between the last two $\pi/2$ pulses. Such an experiment probes the transfer of z magnetization between dipolar-coupled spins via spin diffusion during the mixing time (Xue et al. 2008). Whereas protons that are isolated from one another (e.g., those belonging to different phases) yield only diagonal peaks (peaks with the same frequency in both dimensions), a pair of dissimilar protons that are dipolar-coupled (due to spatial proximity) can produce both diagonal and cross peaks (peaks that are located at different frequencies in the two dimensions), provided a sufficient mixing time is allowed. The intensity ratio between the cross peak and diagonal peak increases with mixing time at a rate that depends on the H-H distance, and ultimately levels off as spin diffusion approaches an equilibrium state. Thus, the spin diffusion

Table 1. Synthesis conditions and run products for representative samples

Sample*	*P*, *T*, and duration	Capsule	Run product‡
K070715	13.5 GPa, 1500 °C, 0.5 h	1.4 mm (OD) Ag-Pd, unsealed	Tpz I > Tpz II (+ minor Sti+Crn)
K071126	14 GPa, 1400 °C†, 1 h	1.4 mm (OD) Ag-Pd, unsealed	Tpz II (+ minor Sti)
K080926b	14 GPa, 1400 °C, 0.5 h	2 mm (OD) Pt, sealed	Tpz I > Tpz II (+ minor Sti)
K080927	13.5 GPa, 1300 °C, 1 h	2 mm (OD) Pt, sealed	Tpz II (+ quench fluid)
K081113	7 GPa, 640 °C†, 3 h	3 mm (OD) Pt, sealed	Tpz I (+minor Coe+Crn+Dsp)

* All synthesized from a mixture of $2Al_2O_3$+$2Al(OH)_3$+$3SiO_2$ using SPEED1500 at SPring-8; all samples (e.g., K071126) are labeled according to the name of experimenter (K for Kanzaki) and the date of synthesis (071126 for November 26, 2007).
† Temperature estimated from the heating power.
‡ Identified by combined micro-Raman, ^{1}H and ^{29}Si NMR, and electron microprobe analysis. Tpz I = topaz-OH I, Tpz II = topaz-OH II, Sti = stishovite, Coe= coesite, Crn= corundum, Dsp = diaspore.

TABLE 2. Chemical compositions from electron microprobe analysis

Phase*	SiO_2 (wt%)	Al_2O_3 (wt%)	Total (wt%)	Si/Al (atomic)
K081113, 7 GPa, 640 °C, 3 h				
Tpz I (20)	33.98(0.99)	54.55(0.97)	88.53(1.11)	0.53(0.02)
Coe (8)	99.66(1.47)	0.10(0.04)	99.76(1.44)	
K070715, 13.5 GPa, 1500 °C, 0.5 h				
Tpz I, grain 1 (20)†	31.26(0.40)	59.75(0.45)	91.00(0.49)	0.44(0.01)
Tpz I, grain 2 (12)†	30.56(0.39)	60.69(0.82)	91.25(0.57)	0.43(0.01)
Tpz II, grain 2 (2)†	30.33(0.07)	61.70(0.09)	92.03(0.16)	0.42(0.00)
Crn, grain 2 (8)†	0.36(0.07)	99.46(0.64)	99.82(0.61)	0.00(0.00)
K080926b, 14 GPa, 1400 °C, 0.5 h				
Tpz I (20)	31.35(0.44)	58.72(0.62)	90.08(0.67)	0.45(0.01)
Sti (12)	97.11(0.88)	3.35(0.89)	100.45(0.58)	25.99(5.73)
K071126, 14 GPa, 1400 °C, 1 h				
Tpz II (20)	31.72(0.56)	58.54(0.86)	90.27(1.17)	0.46(0.01)
K080927, 13.5 GPa, 1300 °C, 1 h				
Tpz II (25)	30.10(0.34)	62.71(0.39)	92.81(0.44)	0.41(0.01)

* Numbers in parentheses are the number of points averaged. Notation for phases as in Table 1.
† Results for two polycrystalline grains (~1 mm size) reported separately.

experiment is particularly useful for evaluating whether a distribution of chemical shifts is caused by structural disorder in a homogeneous phase, or by multiple coexisting phases. For each experiment, eight scans were acquired (and averaged) for 128 pairs of complex t_1 data points with an increment of 101 µs, and a recycle delay time of 3–6 s. The Sates-Haberkorn-Ruben (hypercomplex) method was used to achieve quadrature detection in t_1. Samples were restricted to 0.5–2 mm length near the center of the rotor with Kel-F spacers to improve the RF homogeneity across the sample, because of the known sensitivity of CRAMPS experiments to RF inhomogeneity (Xue and Kanzaki 2007). The scaling factor (0.59–0.61) for the CRAMPS dimension has been calibrated directly on each sample by repeating the measurement with three different offset frequencies; the peak maximum position in the CRAMPS dimension was set to that of the MAS spectrum obtained at the highest spinning rate (35–40 kHz). The CRAMPS chemical shift scale has been corrected for all the reported spectra.

^{27}Al MAS NMR spectra were obtained at a spinning rate of 22 kHz using a Varian 2.5 mm MAS probe with an Al-free zirconia rotor. A spectral width of 2 MHz, a pulse width of 0.2–0.3 µs (about 30° tip angle for selective central transition) and a recycle delay time of 0.2 s were used. Background signal from the rotor and probe was insignificant. A spline correction has been applied to remove the rolling baseline resulting from spectrometer deadtime (ca. 3 µs).

Because ^{27}Al MAS NMR spectra suffer from second-order quadrupolar broadening as a result of the 5/2-spin of ^{27}Al, we have also obtained high-resolution 2D ^{27}Al triple-quantum (3Q) MAS NMR spectra using the three-pulse z-filter sequence described by Amoureux et al. (1996b). Proton decoupling was applied throughout the sequence using the TPPM (two-pulse phase modulation) method (Bennett et al. 1995). Most of the spectra (for samples K081113, K071126, and K080927) have been obtained using a Varian 2.5 mm T3 MAS probe at a spinning rate of 20 kHz and a RF field of 120 kHz for both the 3Q excitation and 3→0Q reconversion pulses (with corresponding optimized pulse lengths of 2.8 and 1.0 µs, respectively). Additional ^{27}Al 3Q MAS NMR spectra were also obtained (for samples K071126 and K080926b) with a Varian 1.6 mm T3 MAS probe at a higher spinning rate of 30 kHz and a higher RF field of 208 kHz for 3Q excitation and reconversion (with corresponding pulse lengths of 1.9 and 0.7 µs, respectively). The pulse length for the third soft z-filter $\pi/2$ pulse was typically set to 8–14 µs. A delay of 10 or 20 µs was kept between the last two pulses. About 1400–9600 scans were acquired (and averaged) for 32–64 pairs of complex t_1 data points with an increment of 25 or 50 µs (one-half or one rotor period) at 20 kHz MAS and 33 µs (one rotor period) at 30 kHz MAS, and a recycle delay time of 0.5 s. The Sates-Haberkorn-Ruben method was used to achieve quadrature detection in t_1. Chemical shift reference in the isotropic dimension follows the convention of Amouroux and Fernandez (1998).

Simulations of the 1D ^{27}Al MAS NMR spectra and the MAS cross-sections of 2D 3Q MAS NMR spectra were performed with the STARS software, taking into considerations of the finite spinning rate and probe bandwidth (about ±0.6 MHz).

^{1}H-^{27}Al cross-polarization (CP)-MAS NMR spectra have also been obtained for all samples at contact times of 1–2 ms, a recycle delay of 0.5–6 s and a spinning rate of 20 kHz using a Varian 2.5 mm T3 MAS probe. A low RF field strength (ca. 9 kHz) for the ^{27}Al channel and a ramped power for the ^{1}H channel (with a RF field range of about 3.5 kHz) were used during CP to improve the CP efficiency (cf. Vega 1992) and stability. Selected samples were measured both with and without proton decoupling during acquisition, and no differences in peak shape were found. About 400–15 000 scans were averaged for each sample.

Because of the small sample sizes (4–20 mg) and low natural abundance (4.7%) and long T_1 for ^{29}Si, sufficient signal/noise could not be achieved for ^{29}Si MAS NMR spectra to allow quantitative detection of small, but important structural features. Fortunately, high-quality ^{1}H-^{29}Si CP-MAS NMR spectra are easily obtainable and have been acquired for all samples using a Varian 2.5 mm T3 MAS probe. A ramped power for the ^{29}Si channel (with a RF field range of about 3.5 kHz), a recycle delay of 3–6 s ($\geq 3T_1$, or $>1.25T_1$ with 2–4 steady-state pulses before acquisition), a range of contact times of 4–20 ms, and a spinning rate of 20 kHz (and also 5, 10, and 15 kHz for some samples) were used. Selected samples of topaz-OH I and II were measured both with and without proton decoupling during acquisition, and no differences in peak shape were found. About 24 000–54 000 scans have been averaged for the reported spectra.

For all CP experiments, the MAS-modified Hartman-Hahn (–1 spinning sideband) condition was used. Spin temperature inversion was incorporated in the phase cycle to eliminate direct polarization, which was confirmed by null experiments on selected samples with the RF power on the ^{1}H channel set to zero during CP.

RESULTS

Phase identifications and chemical compositions

Five samples synthesized at SPring-8 are described in detail (see Table 1), although several additional samples from preliminary experiments have also been studied and yielded similar

TABLE 3. ^{1}H, ^{29}Si, and ^{27}Al NMR results

Sample	Phase(s)†	^{1}H NMR				^{29}Si NMR				^{27}Al NMR				
		δ_i^H (ppm)	FWHM* (ppm)	T_1 (s)	Si site	δ_i^{Si} (ppm)	FWHM (ppm)	population (%)	Al site	δ_i^{Al} (ppm)	P_Q (MHz)	C_Q (MHz)	η_Q	population(%)
K081113	Tpz I	3.8	1.7	0.86	Si^{IV}	–83.4	0.63	100	Al^{VI}	8.2	5.4	5.3	0.4	100
	Dsp	9.4												
K070715	Tpz I+II	4.1§		1.1	Si^{IV}	–83.2§		85	Al^{VI}					
					Si^{VI}	–133, –178§		15	Al^{IV}					
	Tpz I	4.0‡			Si^{IV}	–83.2§		97.3(1)‡	Al^{VI}					
					Si^{VI}	–133§		2.7(1)‡	Al^{IV}					
K080926b	Tpz I+II	3.9§		1.6	Si^{IV}	–83.2§		89	Al^{VI}					98.4
					Si^{VI}	–133, –178§		11	Al^{IV}					1.6
	Tpz I	3.9‡			Si^{IV}	–83.2§		97.2(1)‡	Al^{VI}					>98.4
					Si^{VI}	–133§		2.8(1)‡	Al^{IV}					<1.6
K071126	Tpz II	4.9§	5.0	1.3	Si^{IV}	–80.3§		63(1)	Al^{VI}	12‖	4.5‖			97.8(1)
					Si^{VI}	–177.7§		37(1)	Al^{IV}	68‖	3.5‖			2.2(1)
K080927	Tpz II	4.8§	4.5	4.4	Si^{IV}	–80.6§		67	Al^{VI}	12‖	4.5‖			96.8(1)
					Si^{VI}	–177.6§		33	Al^{IV}	68‖	3.7‖			3.2(1)

* FWHM at a spinning rate of 40 kHz and a magnetic field of 9.4 T.
† Notation for phases as in Table 1.
‡ Estimated from difference spectra after substracting that of topaz-OH II.
§ Maximum of asymmetric peak.
‖ Estimated at the maximum of total projection in the isotropic dimension of 2D 3Q MAS NMR spectra.

results. All samples were initially crushed to coarse grains, and the entire samples were used for detailed multi-nuclear NMR study, except where explicitly noted. Selected pieces of each sample were then embedded in epoxy and polished for chemical analysis and mapping with an electron microprobe. Micro-Raman measurements were performed at various stages: on the recovered sample block before taking it out of the capsule, on the crushed grains, and on the epoxy mount after electron microprobe analysis. Additional NMR measurements on a sample with coexisting topaz-OH I and II (K070715) were also performed after coarse polycrystalline grains containing topaz-OH II were identified by micro-Raman and separated. Powder XRD was performed on fine powders of selected samples after the above detailed characterization (Kanzaki 2010).

Phases other than the two polymorphs of topaz-OH (and SiO_2) can be distinguished by any of these techniques. The distinction between the latter cannot be made from electron microprobe analysis, because of their similar compositions (see below), but relied on micro-Raman and NMR (and XRD). A combined micro-Raman and electron microprobe analysis was used to determine the compositions of topaz-OH I and II from the same sample (e.g., K070715).

Sample K081113 was synthesized at 7 GPa and 640 °C for 3 h and contains submicrometer-sized grains of topaz-OH I with some coesite (SiO_2) and corundum (Al_2O_3), and minor diaspore (AlOOH). All the other samples (originally all aimed at synthesizing topaz-OH II) were produced at a narrow range of higher *P-T* (13.5–14 GPa and 1300–1500 °C) for 0.5–1 h, and consist dominantly of large-grained topaz-OH polymorphs. Sample K071126 (synthesized at 14 GPa and 1400 °C for 1 h) comprises large-grained (on the order of 100 μm) topaz-OH II and minor stishovite (SiO_2). Sample K080927 (synthesized at 13.5 GPa and 1300 °C for 1 h) contains very large clear crystals (several millimeters) of topaz-OH II along with fine ash-like powder (consisting of silica, alumina, and topaz-OH phases as revealed by micro-Raman) that was most likely quench crystals from a fluid phase. The large crystals were carefully picked out and subjected to all the described measurements. Electron microprobe analysis and mapping of selected grains suggest that they are compositionally homogeneous and free of any inclusions. Sample K070715 (synthesized at 13.5 GPa and 1500 °C for 0.5 h) and sample K080926b (synthesized at 14 GPa and 1400 °C for 0.5 h) both consist of large grains (up to ca. 100 μm) of topaz-OH with finer-grained stishovite along grain boundaries. Minor corundum was also observed. Both NMR and Raman (on coarse polycrystalline grains) revealed that the topaz-OH in both samples is dominantly phase I, but some grains contain phase II. The observation of topaz-OH II with and without coexisting topaz-OH I in samples synthesized at the narrow *P-T* range of 13.5–14 GPa and 1300–1500 °C (including some with nominally the same *P-T*) may be explained by the proximity of the *P-T* condition to the polymorphic phase transition boundary (Kanzaki, unpublished results), coupled with uncertainties of the measured pressure (within ca. ±1 GPa, e.g., due to anvil deformation) and temperature (e.g., within ca. ±100 °C with thermocouple failure), and the presence of thermal gradient (within ca. 100 °C across the sample).

The chemical compositions of constituent phases from electron microprobe analysis are reported in Table 2. The composition of topaz-OH I synthesized at 7 GPa and 640 °C (K081113) is close to the ideal $Al_2SiO_4(OH)_2$ composition with a Si/Al ratio of 0.53(2). The standard deviations for this sample are larger than those for all others because of fine grain sizes. The compositions of both topaz-OH I and II in samples synthesized at higher *P-T* (13.5–14 GPa and 1300–1500 °C) exhibit lower-than-ideal Si/Al ratios (0.41–0.46). Topaz-OH II synthesized at 13.5 GPa and 1300 °C (K080927) and 14 GPa and 1400 °C (K071126) give Si/Al ratios of 0.41(1) and 0.46(1), respectively. For sample K070715 (synthesized at 13.5 GPa and 1500 °C), which contains both topaz-OH I and II, the compositions of the two polymorphs are indistinguishable within analytical uncertainties, with Si/Al ratios of 0.43(1) for topaz-OH I and 0.42 for topaz-OH II. For the other sample containing mixed topaz-OH I and II (K080926b) synthesized at 14 GPa and 1400 °C, only the dominant topaz-OH I phase was analyzed by electron microprobe, and give a Si/Al ratio of 0.45(1). The lower-than-ideal Si/Al ratios for topaz-OH in all these high *P-T* samples, which were synthesized from a (nominally) ideal topaz-OH starting composition, are consistent with the presence of coexisting stishovite (except K080927 that contains quenched fluid, instead).

The compositional trend described above is in agreement with those observed for several other samples synthesized from preliminary experiments at ISEI using starting compositions of $AlSiO_3OH$ or $Al_2SiO_4(OH)_2$. For example, a previously described sample (denoted as F050612 here) synthesized by H.F. from a starting composition of $AlSiO_3OH$ at about 12 GPa (with larger uncertainties than experiments described in the present study) and 1200–1300 °C, which consists of topaz-OH (I > II, see below) + kyanite + stishovite, gave a Si/Al ratio of 0.43(2) for topaz-OH I (Xue et al. 2006). Another previously described sample (denoted as I051105 here) produced by Eiji Ito from a starting composition of $Al_2SiO_4(OH)_2$ at ~11 GPa (with larger uncertainties than experiments described in the present study) and 1000 °C (±about 200 °C due to instability in temperature control) contained regions of phase egg + corundum (+quenched fluid nearby) → topaz-OH II (+minor phase egg) → topaz-OH I (+minor phase egg) in one fragment [that was revealed by combined electron microprobe compositional (Si and Al) mapping and micro-Raman mapping] as a result of thermal gradient (possibly in the order of decreasing *T*). The compositions of topaz-OH of both polymorphs and in different parts of the fragment were indistinguishable [Si/Al = 0.43(2) for topaz-OH I, 0.41(2) for topaz-OH II] (Kanzaki et al. 2006). Unpublished data for several other samples also give similar results.

Therefore, it appears that the compositions of topaz-OH are close to the ideal $Al_2SiO_4(OH)_2$ composition at relatively low *P-T* (7 GPa and 640 °C) (for topaz-OH I), but show lower and slightly varying Si/Al ratios (0.41–0.46) at elevated *P-T* (for both topaz-OH I and II). Although no time-series experiments have been performed to evaluate the attainment of equilibrium in these synthesis experiments, all threads of evidence suggest that the phase relation and compositional trends described above most likely reflect the equilibrium state. For samples synthesized at 13.5–14 GPa and 1300–1500 °C for 0.5–1 h (all but one), these include the large grain sizes for topaz-OH (up to ca. 100 μm to several millimeters), the homogenous compositions of all analyzed

phases in a given sample, the systematically low Si/Al ratios for all topaz-OH samples synthesized at high *P-T*, the even distribution of finer-grained stishovite along grain boundaries (formed from excess silica un-incorporated in the topaz-OH structure), and the expected fast kinetics at such high *P-T* conditions (Ono 1999). For the single sample (K081113) synthesized at a lower *P-T* of 7 GPa and 640 °C for 3 h, although the reaction kinetics is expected to be slower than the above, the obtained results are consistent with those for topaz-OH synthesized from similar starting compositions (Al_2O_3-SiO_2-H_2O system with Si/Al ≥ 0.5) at similar or somewhat higher *P-T* (up to 10 GPa and 1000 °C) with longer durations (Northrup et al. 1994; Wunder et al. 1993). Reversal phase transition between topaz-OH I and II has also been confirmed by in situ XRD measurements using synchrotron radiation at SPring-8 (Kanzaki, unpublished results).

Coexisting stishovite in samples produced at high *P-T* generally contain some Al_2O_3 [e.g., ca. 3 wt% Al_2O_3 for K080926b synthesized at 14 GPa and 1400 °C (Table 2); also see Xue et al. 2006 for the example of F050612 described above]. Coexisting corundum (e.g., in K070715 synthesized at 13.5 GPa and 1500 °C) contain negligible SiO_2 (see Table 2). Both observations are consistent with previous studies (e.g., Ono 1999; Pawley et al. 1993) and lend additional support for the equilibrium compositions of these samples.

Raman spectra

Typical unpolarized Raman spectra for the two topaz-OH polymorphs are shown in Figure 1. Raman spectra for topaz-OH I has been previously reported for a sample synthesized at 10 GPa and 800 °C by Komatsu et al. (2005) and for a sample (F050612) synthesized at ca. 12 GPa and 1100–1200 °C by Xue et al. (2006). Shown in Figure 1 are the Raman spectra for topaz-OH I from samples K081113 (synthesized at 7 GPa and 640 °C) (Figs. 1g–1h) and K070715 (synthesized at 13.5 GPa and 1500 °C) (Figs. 1e–1f). Within the O-H stretching region, there are two main bands near 3520 and 3591 cm^{-1} and a weak tail near 3443 cm^{-1}, with relative intensities varying among grains for a given sample. Within the 200–1500 cm^{-1} region, bands near 286, 359, 826, 876, 893, 949, 1135, and 1183 cm^{-1} are observed. The bands near 1135 and 1183 cm^{-1} may be attributed to in-plane O-H bending vibration. These spectra, along with those of topaz-OH I in all other samples from this study, are in general similar to those reported for topaz-OH I previously (Komatsu et al. 2005; Xue et al. 2006). There is also a pair of strong bands near 1360 and 1595 cm^{-1} (Fig. 1g) and a weak band near 2950 cm^{-1} occurring only in the spectra for sample K081113 (Fig. 1h). The former two may be attributed to poorly crystallized graphite, possibly produced due to minor carbon impurities in the starting material (Kanzaki 2008). The latter may be attributed to minor coexisting diaspore from comparison with Raman spectra for single-phased diaspore samples (Kanzaki, unpublished data).

Raman spectra for topaz-OH II in all the samples show a single, asymmetric, broad O-H stretching band near 3500 cm^{-1} that extends to lower frequencies than those of topaz-OH I (see Figs. 1b and 1d for examples of samples K080927 and 070715). From the known correlation between O-H stretching frequency and hydrogen-bonding distance (Libowitzky 1999; Nakamoto et al. 1955), this indicates a distribution of, and overall shorter

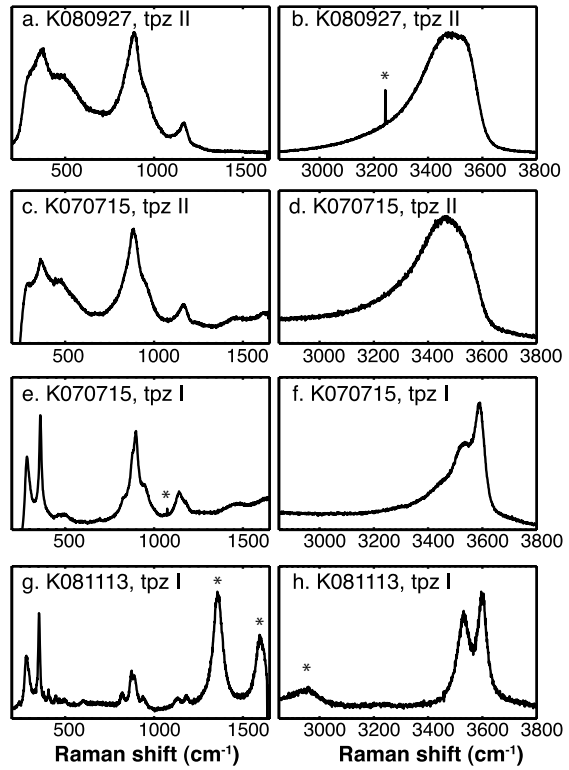

FIGURE 1. Unpolarized Raman spectra of topaz-OH II from sample K080927 (**a**, **b**) and sample K070715 (**c**, **d**), and topaz-OH I from sample K070715 (**e**, **f**) and sample K081113 (**g**, **h**). The two peaks marked by asterisks in **g** are due to carbon contaminant, and that marked by asterisk in **h** may be due to coexisting diaspore. Sharp spikes marked by asterisks in **b** and **e** are due to cosmic rays.

hydrogen-bonding distances in topaz-OH II, as compared to topaz-OH I. The intensity distribution within the broad envelope varies with grains within a given sample, suggesting the presence of orientation-dependency. Within the 200–1500 cm^{-1} region, there are bands near 300, 365, 460, 884 (with a high-frequency shoulder), and 1160 cm^{-1}, which show general resemblance to the corresponding bands of topaz-OH I, but are all broader (see Figs. 1a and 1c for examples of samples K080927 and 070715). This suggests that there is some structural disorder for topaz-OH II, but the overall structure likely resembles that of topaz-OH I.

It should also be mentioned that in some samples that contain both polymorphs of topaz-OH [e.g., K070715, also I051105 described in Kanzaki et al. (2006)], mapping with micro-Raman clearly revealed that there is a clear-cut boundary between the two polymorphs, each with a distinct Raman pattern. Therefore the two polymorphs cannot be regarded as a single phase with a continuous structural variation, but rather are two distinct phases that each has a unique, but related crystal structure (also see Kanzaki et al. 2006).

^{1}H MAS and CRAMPS-MAS NMR spectra

^{1}H MAS NMR spectra were obtained for all samples at a range of spinning rates from 10 kHz to 35–40 kHz. Typical ^{1}H MAS NMR spectra acquired at a spinning rate of 35 kHz for all samples are shown in Figure 2. The ^{1}H MAS NMR spectrum for sample K081113 (7 GPa and 640 °C) (that contains topaz-OH

I as the dominant (hydrous) phase) acquired at a spinning rate of 40 kHz exhibits a main, symmetric peak near 3.8 ppm with a full-width at half maximum (FWHM) of 1.7 ppm, attributable to topaz-OH I (Xue and Kanzaki 2009). The FWHM increases nearly linearly with increasing $1/\nu_R$ and becomes 3.0 ppm at a spinning rate, ν_R of 20 kHz and 4.9 ppm at ν_R = 10 kHz, suggesting that the peak width is dominated by ^{1}H-^{1}H homonuclear dipolar coupling (Xue and Kanzaki 2009). There is also a very weak, broader peak near 9.4 ppm, which may be attributed to minor coexisting diaspore (Xue and Kanzaki 2007), consistent with the Raman result.

The ^{1}H MAS NMR spectra acquired at a spinning rate of 40 kHz for samples K071126 (14 GPa and 1400 °C) and K080927 (13.5 GPa and 1300 °C) (that contain topaz-OH II as the only hydrous phase as revealed by micro-Raman and XRD) each show a broad asymmetric peak with a narrower component near the maximum at 4.8–4.9 ppm and a high-frequency tail that extends to much higher frequency (ca. 12 ppm) than that of topaz-OH I described above (ca. 7 ppm), all attributable to topaz-OH II. The narrower component is somewhat more prominent for sample K080927 than sample K071125, suggesting subtle local structural variation around protons in topaz-OH II with *P-T*. The FWHM increases with decreasing spinning rate for both samples (e.g., from 4.5 ppm at ν_R = 40 kHz to 5.3 ppm at ν_R = 20 kHz for K080927), although the changes are less prominent than that of topaz-OH I described above. This suggests that the broad peak width is likely caused not only by ^{1}H-^{1}H homonuclear dipolar coupling, but also by a distribution of chemical shifts.

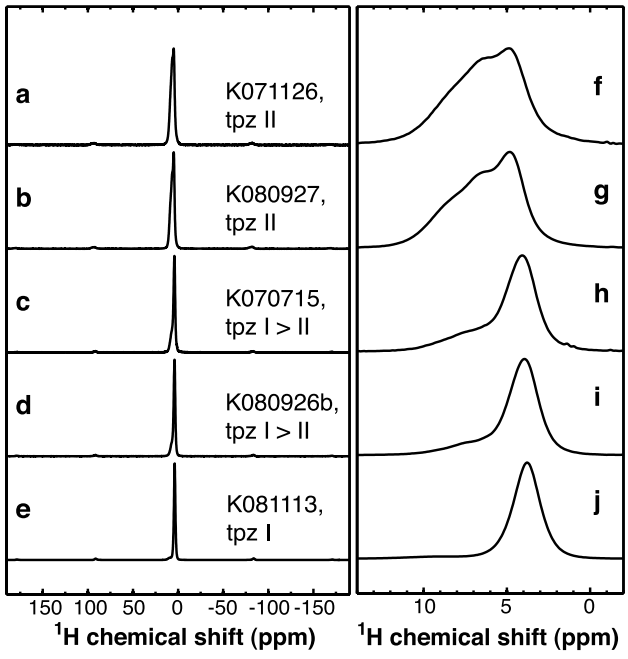

FIGURE 2. ^{1}H MAS NMR spectra (**a**–**e**: wider frequency range; **f**–**j**: around the central band region) for samples containing topaz-OH I (K081113), topaz-OH II (K080927, K071126), and those containing both polymorphs (K080926b and K070715), acquired at a spinning rate of 35 kHz, a spectral width of 1 MHz, a recycle delay time of 3–15 s ($\geq 5T_1$). A small Gaussian line broadening function with a time constant of 0.01 s (that barely affected the peak width) has been applied to all.

The ^{1}H MAS NMR spectra acquired at a spinning rate of 35 kHz for samples K070715 (13.5 GPa and 1500 °C) and K080926b (14 GPa and 1400 °C) (that consist dominantly of topaz-OH I with some topaz-OH II as revealed by micro-Raman) each contain a dominant narrow peak with a maximum near 3.9–4.1 ppm and a broader high-frequency tail (Figs. 2h–2i). The former is close to that of topaz-OH I (Fig. 2j), and the latter matches well with that of topaz-OH II described above (also see Figs. 2f–2g). To further constrain the origin of these two components, coarse (polycrystalline) grains of sample K070715 were examined by micro-Raman and those grains that gave Raman pattern of topaz-OH II were separated and subjected to further ^{1}H MAS NMR measurements. It was found that the broad high-frequency tail is more prominent in such grains (see Fig. 3a), suggesting that it indeed originates from topaz-OH II. The main, narrower peak near 3.9–4.1 ppm may be attributed to topaz-OH I, as is clear from the difference spectrum taken between the (bulk) sample K070715 and topaz-OH II-enriched grains of the same sample (Fig. 3a), and the difference spectra taken between either of samples K070715 and K080926b (topaz-OH I + II) and either of samples K071126 and K080927 (topaz-OH II only) (see Figs. 3b–3c for examples), which all resemble the peak shape of topaz-OH I from sample K081113 (see Fig. 2j). Note that in taking the difference spectra, the relative intensities of the two relevant spectra have been adjusted so that the difference spectrum contains minimal (sum of squared) intensities in a frequency range (7–13 ppm) where only topaz-OH II (but not topaz-OH I) is expected, similar to the procedure described in Malfait and Xue (2010). Therefore, both Raman and ^{1}H MAS NMR are consistent with the coexistence of topaz-OH I and II in these two samples. Topaz-OH II is somewhat more abundant in sample K070715 than sample K080926b, as is clear from the ^{1}H MAS NMR spectra (Figs. 3b–3c).

It is worth mentioning that although most of the samples contain minor stishovite, which is known to accommodate trace amount of water and contribute to a narrow ^{1}H peak near 9.3 ppm (Xue et al. 2006), no narrow peak attributable to stishovite can be resolved in all the ^{1}H MAS NMR spectra shown in Figure 2. This is a combined result of small quantity of stishovite and saturation due to its much longer ^{1}H T_1 [e.g., 142 s for a sample measured in Xue et al. (2006)] than the recycle delay times (3–15 s) used. We have, in fact, observed a peak near 9.3 ppm for stishovite in ^{1}H MAS NMR spectra acquired with longer recycle delay times ($\geq$200 s) for several other topaz-OH samples containing more abundant coexisting stishovite [synthesized from a starting composition of $AlSiO_3OH$ in preliminary experiments, e.g., F050612 described in Xue et al. (2006)].

To place further constraint on the proton order-disorder in topaz-OH I and II, 2D ^{1}H CRAMPS-MAS NMR spectra were also obtained at a spinning rate of 15 kHz and with mixing times of 2 μs and 200 ms using the FSLG homonuclear decoupling scheme (Bielecki et al. 1989; Xue and Kanzaki 2007). This technique has proven particularly useful in ascertaining the presence/absence of proton disorder in high-pressure minerals (e.g., phase D, δ-AlOOH) (Xue and Kanzaki 2007; Xue et al. 2008). Typical 2D ^{1}H CRAMPS-MAS NMR spectra for samples containing topaz-OH I (K081113), topaz-OH II (K080927), and both polymorphs (K080926b) are shown in Figure 4. The 2D ^{1}H

CRAMPS-MAS NMR spectrum of topaz-OH I (K081113) (with a minimal mixing time of 2 μs) contains a narrow, symmetric peak with a FWHM of 0.3 ppm (after scaling correction) for the total projection in the CRAMPS dimension, suggesting no detectable proton local structural disorder (Fig. 4e).

The 2D ^{1}H CRAMPS-MAS NMR spectrum of topaz-OH II (K080927) acquired with a mixing time of 2 μs, on the other hand, exhibits a broad peak elongated along the diagonal with a distribution of frequencies in both the MAS and high-resolution CRAMPS dimensions, suggesting that there is a distribution of chemical shifts (Fig. 4a). For the spectrum acquired at a longer mixing time of 200 ms (Fig. 4b), cross-peak intensities are developed among the entire frequency range of the broad peak, so that the broad peak is now aligned parallel to the axis with cross-sections taken at different positions giving identical peak shape (not shown). This is a clear indication that the different parts of the broad peak belong to a single, homogeneous phase (with a range of local structures around protons, i.e., proton disorder), rather than spatially separate phases (e.g., multiple coexisting phases, inclusions, or a single phase with spatial compositional/structural heterogeneity). Spin diffusion among all the protons has reached equilibrium with a mixing time of 200 ms, as was previously observed for phase D (Xue et al. 2008). Similar results have also been obtained for the other sample of topaz-OH II (K071126, not shown).

The 2D ^{1}H CRAMPS-MAS NMR spectra acquired with a mixing time of 2 μs for the two samples with mixed topaz-OH I

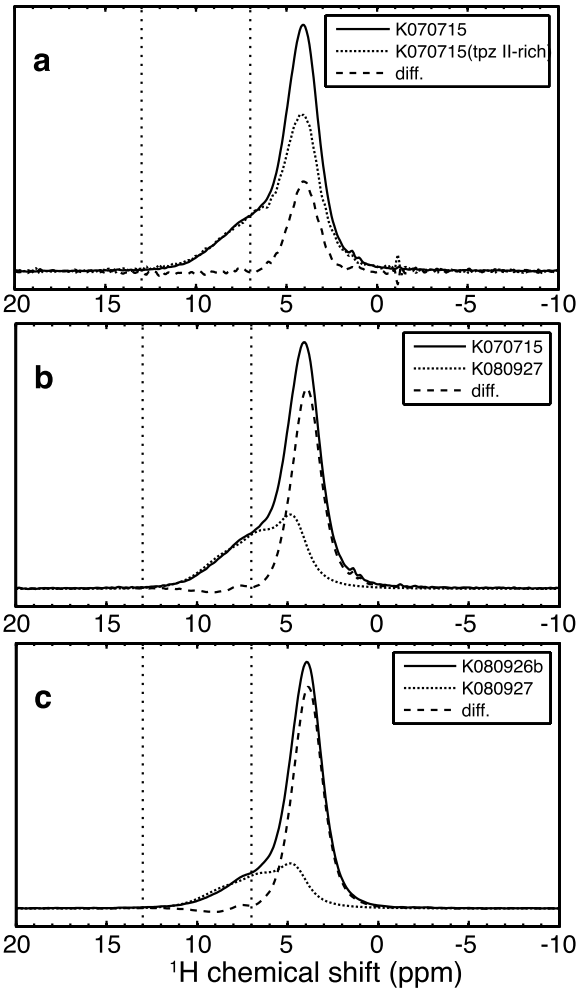

FIGURE 3. (**a**) ^{1}H MAS NMR spectra of sample K070715 (topaz-OH I + II) (solid line) and topaz-OH II-enriched grains of the same sample (dotted line), and the difference spectrum of the two (dashed line); (**b**) ^{1}H MAS NMR spectra of sample K070715 (topaz-OH I + II) (solid line) and sample K080927 (topaz-OH II) (dotted line), and the difference spectrum of the two (dashed line); (**c**) ^{1}H MAS NMR spectra of sample K080926b (topaz-OH I + II) (solid line) and sample K080927 (topaz-OH II) (dotted line), and the difference spectrum of the two (dashed line). All the spectra have been acquired at a spinning rate of 35 kHz, a spectral width of 1 MHz, a recycle delay time of 3–15 s ($\geq 5T_1$). A small Gaussian line broadening function with a time constant of 0.01 s has been applied to all. The relative intensities of the two spectra in each graph have been adjusted so that the sum of squared intensities in a frequency region (delineated by dotted vertical lines) where topaz-OH I is not expected is minimized for the difference spectrum. Further expanding the reference region beyond 7 ppm would yield prominent negative intensity for the difference spectra. Taking the difference with sample K071126 (topaz-OH II), instead, for **b** and **c** yields similar results.

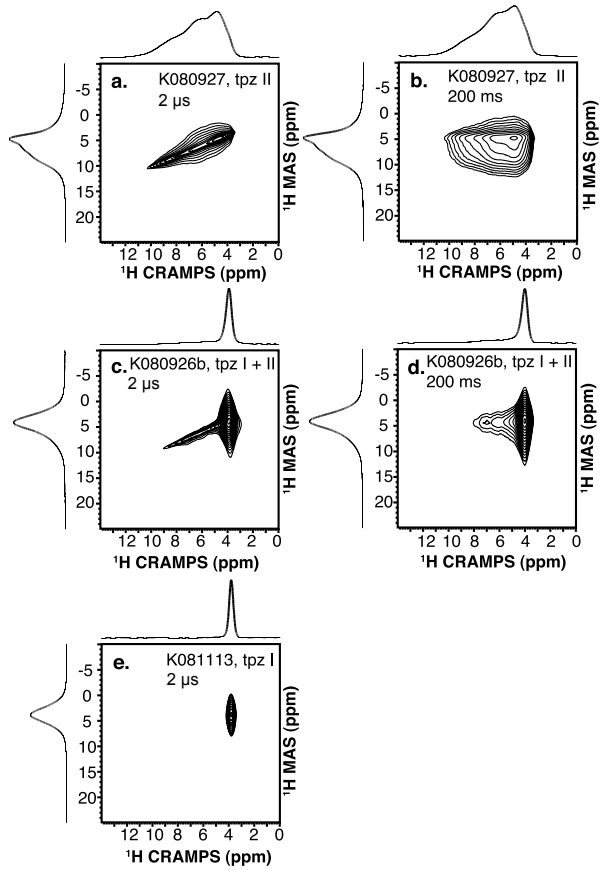

FIGURE 4. 2D ^{1}H CRAMPS-MAS NMR spectra acquired at a spinning rate of 15 kHz, a recycle delay of 3–6 s [$\geq 3T_1$ (**c**–**e**) or $>1.25T_1$ with one steady-state pulse before each acquisition (**a**–**b**)], and mixing times of 2 μs (**a**, **c**, **e**) and 200 ms (**b**, **d**) for samples containing topaz-OH I (K081113) (**e**), topaz-OH II (K080927) (**a**, **b**), and both polymorphs (K080926b) (**c**, **d**). The chemical shift scale in the CRAMPS dimension has been corrected. A small Gaussian line broadening function with a time constant of 0.01 s has been applied to both dimensions. All contours have been plotted in a logarithmic scale with 10 (**a**, **b**, **e**) or 15 (**c**, **d**) levels and a spacing factor of 1.3.

and II (K070715 and K080926b) each show a main component with a narrow peak width in the CRAMPS dimension and a weaker component with a broad distribution of frequencies in both dimensions (see Fig. 4c for the latter sample). The alignment of the latter component is again changed from diagonal at a mixing time of 2 μs (Fig. 4c) to parallel to the axis at a mixing time of 200 ms (Fig. 4d), suggesting that spin diffusion has occurred among the entire frequency range of the broad component. The two components correspond well to peaks of topaz-OH I and II described above.

Therefore, high-resolution 2D ^{1}H CRAMPS-MAS NMR data revealed no detectable proton disorder in topaz-OH I, but provided unambiguous evidence for the presence of considerable proton disorder in topaz-OH II.

^{1}H-^{29}Si CP-MAS NMR spectra

Typical ^{1}H-^{29}Si CP-MAS NMR spectra for all samples acquired with contact times of 4 or 8 ms at a spinning rate of 20 kHz are shown in Figure 5. The ^{1}H-^{29}Si CP-MAS NMR spectra of sample K081113 (topaz-OH I, 7 GPa, 640 °C), acquired with a recycle delay of 3 s, a contact time of 4 ms and a spinning rate of 20 kHz (Fig. 5e) yields a narrow, symmetric peak at –83.4 ppm with a FWHM of 0.63 ppm, attributable to tetrahedral Si (Si^{IV}) in topaz-OH I (Xue et al. 2006). No peaks in the range expected for octahedral Si (–130 to –190 ppm, see below) are detected.

The ^{1}H-^{29}Si CP-MAS NMR spectra of sample K071126 and K080927 (topaz-OH II, 13.5–14 GPa, 1300–1400 °C) acquired with contact times between 4 to 20 ms and spinning rates of 10 and 20 kHz all show an asymmetric peak with a maximum near –80.3 to –80.6 ppm and a tail to higher frequency, which is significantly broader and shifted to higher frequency as compared to that of topaz-OH I for sample K081113. In addition, a smaller, broad peak with maximum near –178 ppm and a high-frequency tail extending to about –130 ppm is also clearly visible (see Figs. 5a, 5b, and 5f). The high spinning rate of 10–20 kHz is critical for the unambiguous identification of the entire frequency range of the latter peak (especially the high-frequency tail to –130 ppm); with lower spinning rates of ≤8 kHz (e.g., 4 kHz as used in Xue et al. (2006), the spinning sideband of the main peak near –80 ppm would partially overlap with the latter peak. As further discussed in the next section, the main peak near –80 ppm is within the range expected for Si^{IV}, and may be assigned accordingly, and the latter may be attributed to octahedral Si (Si^{VI}). To evaluate whether the relative intensities of the two peaks vary with experimental conditions, ^{1}H-^{29}Si CP-MAS NMR spectra have been obtained for sample K071126 at a spinning rate of 20 kHz and contact times of 4, 8, 12, and 20 ms, and at a spinning rate of 10 kHz and a contact time of 4 ms. The relative intensities of the two peaks remain the same for all five spectra, giving an average (with standard deviation in brackets) of 63(1)% for Si^{IV} and 37(1)% for Si^{VI}. Similarity of ^{1}H-^{29}Si CP dynamics for different Si sites have also been previously observed for phase egg ($AlSiO_3OH$) (Xue et al. 2006), and may be attributed to the lack of significant contrast in Si-H distances for all Si sites. Under such a condition, the obtained relative peak intensities may be taken to represent the site abundances. The relative intensities of the two peaks for sample K080927, estimated from a spectrum acquired at a spinning rate of 20 kHz and a contact time of 4 ms are 67 and 33%, respectively. There are subtle differences in peak shapes for both Si^{IV} (peak maximum at slightly higher frequency for K0711126 than K080927) and Si^{VI} (more prominent narrower component near –179 ppm relative to the broad high-frequency tail for K0711126) between the two samples (see Figs. 5a–5b). Together with the observed small differences in relative intensities of the two peaks, in peak shape of the ^{1}H MAS NMR spectra (Fig. 2), and in composition (Si/Al ratio) (Table 2) between the two samples, it may be concluded that the local structure and composition of topaz-OH II vary slightly with *P-T* conditions.

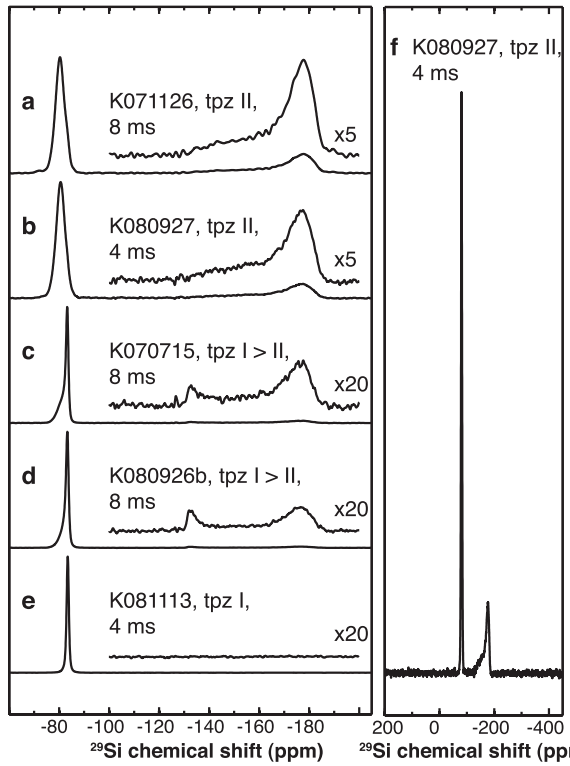

FIGURE 5. ^{1}H-^{29}Si CP-MAS NMR spectra for samples containing topaz-OH I (K081113) (**e**), topaz-OH II (K071126, K080927) (**a**, **b**, **f**), and both polymorphs (K070715, K080926b) (**c**, **d**), acquired with a contact time of 4–8 ms (as marked), a recycle delay time of 3–6 s [$\geq 3T_1$ (**a**, **c**, **e**), or $>1.25T_1$ (**b**, **d**) with 2–4 steady-state pulses before acquisition] and a spinning rate of 20 kHz. Also shown above each spectrum in **a**–**e** is the corresponding spectrum in the range –100 to –200 ppm with vertical scale expanded by 5 or 20× (as marked). Figure **f** is the same as **b**, but is plotted with a wider frequency range for clarity. Other spectra acquired with a range of contact times of 4–20 ms and different recycle delay times for selected samples (e.g., K071126, K081113, K070715) give identical peak shape (relative intensities).

The ^{1}H-^{29}Si CP-MAS NMR spectra of sample K070715 and K080926b (topaz-OH I > II) acquired at a spinning rate of 20 kHz and a contact time of 8 ms both contain a main peak near –83 ppm with a high-frequency shoulder, and a weak broad peak in the –130 to –190 ppm region (with two maxima near –178 and –133 ppm) (Figs. 5c–5d). The main, narrower peak near –83 ppm for both samples is consistent with that of topaz-OH I; the broad asymmetric high-frequency tail of the main peak and the weak peak near –178 ppm both match well with those of topaz-OH II

described above, and may be assigned accordingly. The latter two components are more prominent for sample K070715 (Fig. 5c) than K080926b (Fig. 5d), which may be explained by greater abundance of topaz-OH II in the former, consistent with ^{1}H MAS NMR results described above. The overall relative intensities of the broad peak in the –130 to –190 ppm region are ca. 15% for sample K070715 and 11% for sample K080926b. The spectral feature of topaz-OH I in samples K070715 and K080926b may be roughly estimated by subtracting out the spectra for topaz-OH II (from samples K080927 or K071126). Examples are shown for the comparison of peak shapes of samples K070715 and K080926b (topaz-OH I > II) with that of K080927 (topaz-II) in Figure 6. The relative intensities of the two spectra were adjusted so that the difference spectrum contains minimal (sum of squared) intensities in a frequency range (–72 to –80 ppm) where only topaz-OH II (but not topaz-OH I) is expected. This procedure leads to the maximal subtraction of topaz-OH II-like component, because further moving the frequency limit to < –76 ppm would result in significant negative intensities in the difference spectrum. The difference spectra, which may be taken to approximate the spectra for topaz-OH I, contain a narrow, somewhat asymmetric peak near –83.3 ppm, and a weak broad peak with a maximum near –133 ppm (and possibly a very weak tail to –190 ppm) (see Fig. 6). The estimated relative intensity in the –130 to –190 ppm region for the difference spectra (topaz-OH I) are ca. 2.7(1)% for sample K070715 and 2.8(1)% for K080926b. Like the ^{1}H MAS NMR spectra described above, similar results were obtained if the difference spectra were taken with sample K071126 (topaz-OH II only), instead (not shown), because the difference in peak shape for topaz-OH II between the two samples are only secondary.

It should be pointed out the ^{1}H-^{29}Si CP-MAS NMR spectrum reported in Xue et al. (2006) for a sample synthesized at ca. 12 GPa and 1200–1300 °C (F050612) (topaz-OH + kyanite + stishovite) measured at a spinning rate of 4 kHz similarly also gave an asymmetric peak near –83.3 ppm with a high-frequency shoulder, and a peak near –177 ppm (with an estimated relative intensity of about 7%). The low spinning rate rendered only part of the envelope in the –130 to –190 ppm region recognized (because the first spinning sideband of the main peak is expected to occur near –134 ppm), so that its actual intensity should be somewhat higher. Therefore, this sample most likely also contained dominantly topaz-OH I with some topaz-OH II. NMR was a more sensitive probe of the minor topaz-OH II phase than micro-Raman [which only detected topaz-OH I in Xue et al. (2006)], because it was taken on the bulk sample, rather than selected regions.

Although most of the samples described above contain minor (water-bearing) stishovite, no peak near –191.4 ppm expected for the latter (Xue et al. 2006) has been observed in any of the ^{1}H-^{29}Si CP-MAS spectra (Fig. 5). As discussed in Xue et al. (2006), this is a combined result of small abundance, proton saturation, and low CP efficiency for stishovite.

^{27}Al MAS NMR, ^{27}Al 3Q MAS NMR, and ^{1}H-^{27}Al CP-MAS NMR

Typical ^{27}Al MAS NMR spectra acquired at a spinning rate of 22 kHz and 2D 3Q MAS NMR spectra acquired at a spinning rate of 20 or 30 kHz for all samples are shown in Figures 7 to 10.

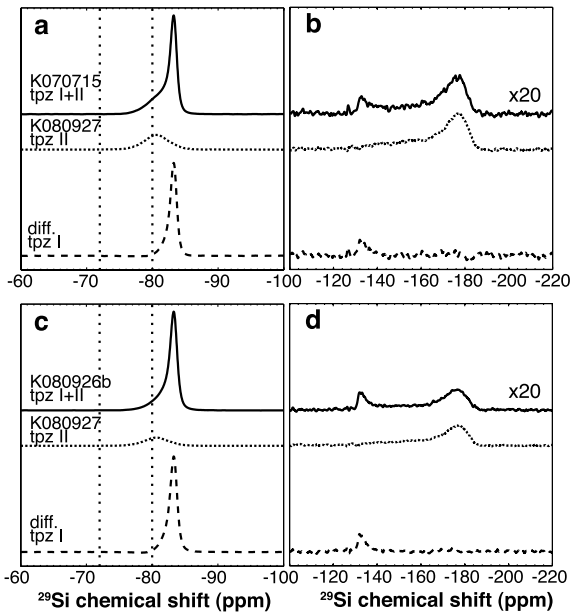

FIGURE 6. Comparison of ^{1}H-^{29}Si CP-MAS NMR spectrum for samples containing topaz-OH I + II [**a**, **b**: K070715 (contact time: 8 ms); **c**, **d**: K080926b (contact time: 8 ms) (top, solid line)] and that containing only topaz-OH II [K080927 (contact time: 4 ms) (middle, dotted line)], all acquired at a spinning rate of 20 kHz (as for Fig. 5), and their difference spectra (bottom, dashed line). The latter were obtained by adjusting the relative intensities of the two spectra so that the sum of squared intensities in the –72 to –80 ppm region (delineated by vertical, dotted lines), where topaz-OH I is not expected, are minimized in the difference spectrum. Further expanding the reference region beyond –80 ppm would yield prominent negative intensity for the difference spectra. All spectra are shown in an expanded vertical scale (20×) in the –100 to –200 ppm region (**b**, **d**) relative to the corresponding spectra in the –60 to –100 ppm region (**a**, **c**).

The ^{27}Al MAS NMR spectrum of sample K081113 (topaz-OH I) contains a central band with sharp maxima near –2.5 and –12.4 ppm (Fig. 7). The ^{27}Al 3Q MAS NMR spectrum of the sample yields a narrow, slightly asymmetric peak with a maximum near 17.7 ppm in the total projection to the isotropic F_1 dimension (Fig. 8a). The MAS (F_2) cross-section taken at the latter position (Fig. 8b) can be well reproduced by a single set of parameters (δ_i^{Al} = 8.2 ppm, C_Q^{Al} = 5.3 MHz, and η_Q^{Al} = 0.4, where δ_i, C_Q, and η_Q are the isotropic chemical shift, quadrupolar coupling constant, and electric field gradient asymmetry parameter, respectively) (Fig. 8c). The spinning sideband intensity pattern of the 1D ^{27}Al MAS NMR spectrum can also be reasonably reproduced by the same set of parameters (Fig. 7a), suggesting the local structural environment around Al in topaz-OH I of sample K081113 is largely ordered. The δ_i^{Al} value of 8.2 ppm is typical of those for octahedral Al [Al^{VI}: –10 to 15 ppm (Stebbins 1995; Xue and Kanzaki 2007)], consistent with the known crystal structure of topaz-OH. The relative intensity of the left maximum near –2.5 ppm for the central band of the ^{27}Al MAS NMR spectrum is, however, somewhat taller than that of the simulated spectrum (Fig. 7b). The extra intensity corresponds to minor, additional components with narrower MAS pattern(s) that contribute to a weak, low-frequency tail of the total projection to the isotropic

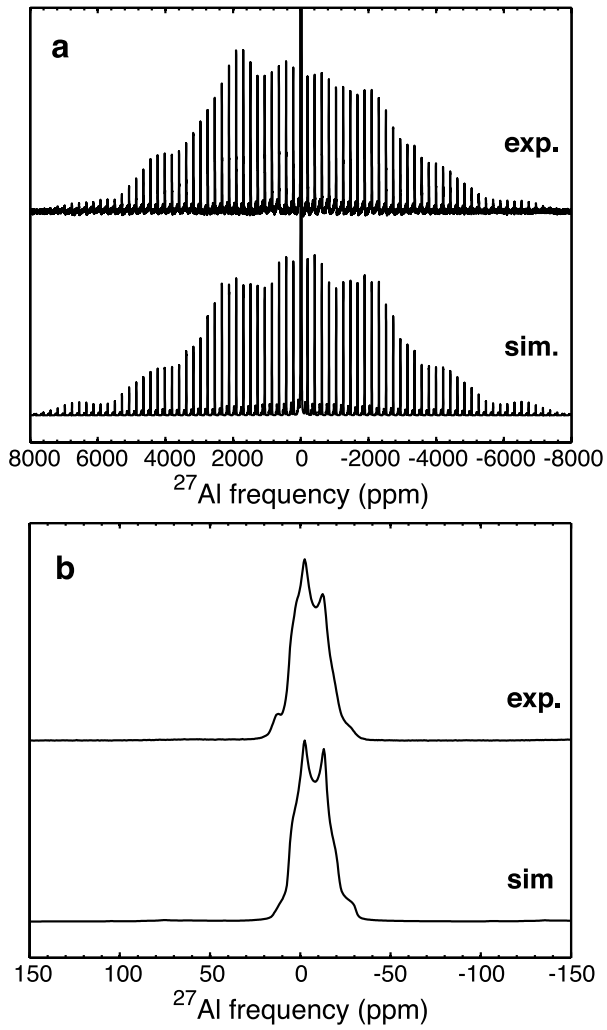

FIGURE 7. ^{27}Al MAS NMR spectra and simulations (**a**: entire spectral range; **b**: around the central band) for sample K081113 (topaz-OH I) acquired with a pulse width of 0.2 μs (ca. 30° tip angle for selective central transition), a recycle delay of 0.2 s, and a spinning rate of 22 kHz with proton decoupling during acquisition. Also shown below the experimental spectrum is the simulated spectrum obtained with $\delta_i^{Al} = 8.2$ ppm, $C_Q^{Al} = 5.3$ MHz, $\eta_Q^{Al} = 0.4$, and a RF band width of ±0.6 MHz.

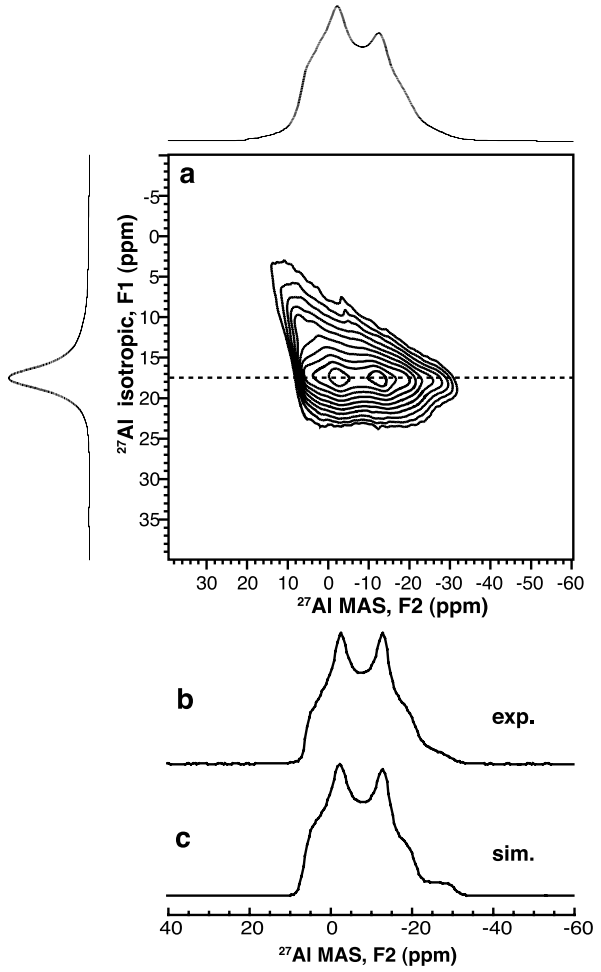

FIGURE 8. Rotor-synchronized ^{27}Al 3Q MAS NMR spectrum with total projections shown along both dimensions for sample K071113 (topaz-OH I) (**a**), the MAS (F_2) cross-section (**b**) taken at the peak maximum in the isotropic (F_1) dimension (denoted by a dotted line in **a**), and the simulated spectrum (**c**) of **b**. The ^{27}Al 3Q MAS NMR spectrum was acquired at a spinning rate of 20 kHz (**a**) with a recycle delay of 0.5 s, a t_1 time increment of 50 μs (one rotor period), and 64 t_1 increments; 1440 scans were averaged. A Gaussian line broadening function with a time constant of 0.01 s has been applied to both dimensions. The contours in **a** have been plotted in a logarithmic scale with 10 levels and a spacing factor of 1.5.

dimension of the 2D 3Q MAS NMR spectrum (Fig. 8a). The extra component cannot be accounted for by minor coexisting corundum or diaspore, because corundum is expected to contribute to a peak near 18 ppm (F_1) and 13 ppm (F_2), and diaspore contribute to a peak near 22 ppm (F_1) and 9 ppm (F_2) in the 2D 3Q MAS NMR spectrum [corundum: $\delta_i^{Al} = 16$ ppm, $C_Q^{Al} = 2.4$ MHz, and $\eta_Q^{Al} = 0$ (cf. Stebbins 1995); diaspore: $\delta_i^{Al} = 17$ ppm, $C_Q^{Al} = 3.4$ MHz, and $\eta_Q^{Al} = 0.8$ (Xue, unpublished data)]. It is tentatively attributed to imperfections in the crystal structure of topaz-OH due to the submicrometer crystallite sizes of the sample produced at a relatively low temperature (640 °C), which may have resulted in local Al structures with a range of (smaller) C_Q^{Al} values.

The ^{27}Al MAS NMR spectra for the two samples of topaz-OH II (K071126 and K080927) each contain an asymmetric peak with a maximum near 4.2–4.6 ppm and a tail to low frequency in the central band region (Fig. 9b). The spinning sidebands for both samples show a bell-shaped intensity pattern (Fig. 9a). Both the peak shape of the central band and the spinning sideband intensity pattern cannot be reproduced by a single set of NMR parameters, but are typical of octahedral Al with a range of parameters (Xue et al. 2006). There is also a smaller shoulder near 50 ppm in the central band region for both samples (Fig. 9b). The two peaks are better resolved in the 2D 3Q MAS NMR spectra (Figs. 10c–10d). The projection to the isotropic (F_1) dimension of the main peak is broad and asymmetric with a maximum near 19 ppm and a tail to higher frequency for both samples (Figs. 10c and 10d), again suggesting the presence of a distribution of local structures around octahedral Al. The distribution of isotropic chemical shift, δ_i^{Al} (in ppm) and quadrupolar products, $P_Q^{Al} (= C_Q \sqrt{1 + \eta_Q^2 / 3})$ (in MHz) may be approximately estimated

from the positions of center of gravity for selected MAS (F_2) cross-sections across the peak in the F_1 projection according to the following (Amoureux and Fernandez 1998):

$$\delta_i^{Al} = \frac{10}{27}\delta_2 + \frac{17}{27}\delta_1$$

$$P_Q^{Al} = 0.010244\nu_0\sqrt{\delta_1 - \delta_2}$$

where δ_1 and δ_2 are the peak positions (in ppm) in the F_1 and F_2 dimensions, respectively, and ν_0 is the resonance frequency (in MHz). Simulation of the MAS cross-section at the maximum of the isotropic projection gives a δ_i^{Al} of 12 ppm and P_Q^{Al} of 4.5 MHz for both samples. Simulations of a range of cross-sections give δ_i^{Al} in a range of 6–17 ppm, while P_Q^{Al} increases systematically from 1 to 11 MHz with increasing F_1 frequency. The obtained δ_i^{Al} values are typical of those for octahedral Al [–10 to 15 ppm: (Stebbins 1995; Xue et al. 2006)]. A similar estimation for the cross-section at the maximum of the isotropic projection of the smaller peak gives a δ_i^{Al} of 68 ppm and P_Q^{Al} of 3.5–3.7 MHz for the two samples (see Table 3). The δ_i^{Al} value is typical of those for tetrahedral Al (Al^{IV}) [50–90 ppm: (Stebbins 1995)]. No additional peak(s) in the 2D ^{27}Al 3Q MAS NMR spectra can be recognized at positions in between the main peak of Al^{VI} and minor peak of Al^{IV}, where peaks of pentacoordinate Al (Al^{V}) are known to occur for many crystalline and glassy aluminosilicates (MacKenzie and Smith 2002). This suggests that Al^{V} species are most likely absent in the topaz-OH structures.

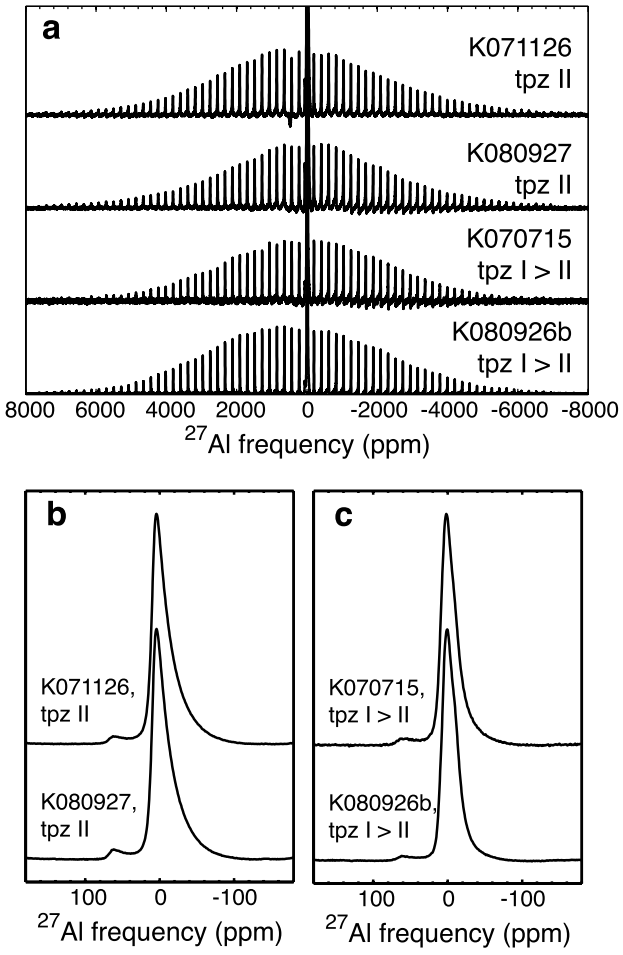

FIGURE 9. ^{27}Al MAS NMR spectra (**a**: entire frequency range; **b**–**c**: central band) of samples K070715 and K080926b (both topaz-OH I > II), and samples K071126 and K080927 (both topaz-OH II), all acquired with a pulse width of 0.2–0.3 µs (ca. 30° tip angle for selective central transition), a recycle delay of 0.2 s, and a spinning rate of 22 kHz with proton decoupling during acquisition.

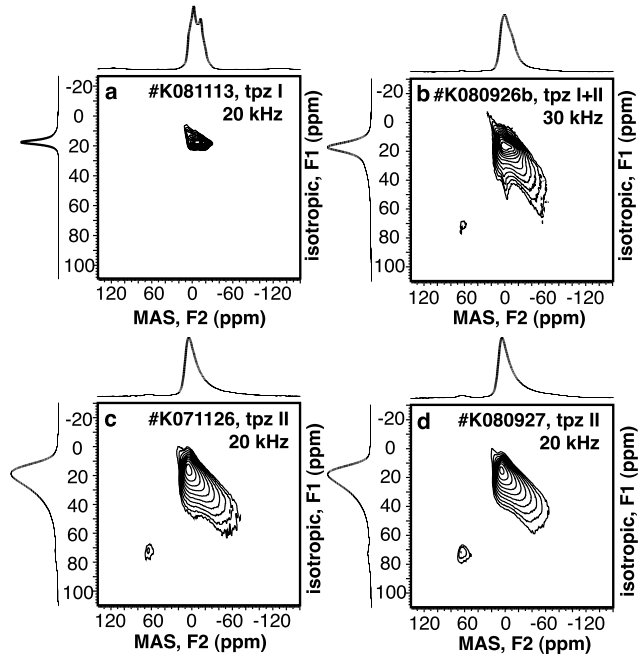

FIGURE 10. Rotor-synchronized ^{27}Al 3Q MAS NMR spectra with total projections along both dimensions for samples K081113 (topaz-OH I) (**a**), K080926b (topaz-OH I > II) (**b**), K071126 (topaz-OH II) (**c**), and K080927 (topaz-OH II) (**d**), acquired at a spinning rate of 20 or 30 kHz (as marked) with a recycle delay of 0.5 s, a t_1 time increment of one (**a**, **b**) or one-half (**c**, **d**) rotor period, and 32 to 64 t_1 increments; 1440 to 7488 scans were averaged for each. A Gaussian line broadening function with a time constant of 0.005 s has been applied to both dimensions. All contours have been plotted in a logarithmic scale with 10 (**a**, **c**, **d**) or 12 (**b**) levels and a spacing factor of 1.5. The sharp diagonal tail near the main peak (for octahedral Al) in **b** is minor artifact (sheared t_2 ridge due to imperfect baseline) that appears prominent because of the expanded vertical scale used to make the weak tetrahedral Al peak visible.

The relative abundance of Al^{IV} may be estimated from the relative peak volume in the 2D ^{27}Al 3Q MAS NMR spectra. Although the relative intensities of peaks in 3Q MAS NMR spectra are in general known to be sensitive to the RF power for the 3Q excitation and reconversion pulses for sites with different C_Q values (Amoureux et al. 1996a), the Al^{VI} and Al^{IV} peaks in these samples have comparable C_Q values, and thus may be close to quantitative. To double check the quantification, 3Q MAS NMR spectra have been obtained for sample K071126 under two different conditions: one at a spinning rate of 30 kHz (rotor-synchronized in the F_1 dimension) using a large RF field of 208 kHz for 3Q excitation and reconversion, and another at a spinning rate of 20 kHz using a smaller RF field of 120 kHz for 3Q excitation and reconversion. The estimated relative volume for Al^{IV} peak are in good agreement with each other [2.2(1)%], and are also comparable to the relative peak height in the 1D MAS NMR spectrum, suggesting that the 3Q excitation efficiencies for the two peaks are indeed similar and

the relative volume closely represents the true abundance. The abundance of Al^{IV} for the other topaz-OH II sample (K080927) is estimated to be 3.2%.

The ^{27}Al MAS NMR spectra for the two samples of topaz-OH I + II (K070715 and K080926b) each contain an asymmetric peak with a maximum near 0.7–1.8 ppm and a tail to low-frequency, attributable to Al^{VI} with a range of NMR parameters, and a shoulder near 50 ppm, attributable to Al^{IV} (Fig. 9c). To get an approximate idea of the peak shape for topaz-OH I in these samples, the ^{27}Al MAS NMR spectra of topaz-OH II (from sample K080927 or K071126) were subtracted from those of the above until the (sum of squared) intensities of the low-frequency tail (–35 to –100 ppm, characteristic of topaz-OH II) is minimized in the difference spectrum (Fig. 11). The resultant peak shapes are similar using either of the reference spectra for topaz-OH II, but differ from that of topaz-OH I in sample K081113, showing no sharp features (see Fig. 11). This suggests the local structures around Al in topaz-OH I have (greater) local Al disorder for these high *P-T* samples than that synthesized at 7 GPa and 640 °C (K081113). There may also be some weak intensity for Al^{IV} in the difference spectrum, although the subtraction procedure is subject to large error, because of uncertainties with phasing for broad peaks. To get a better idea of the abundance of Al^{IV} in the mixed topaz-OH I and II samples, ^{27}Al 3Q MAS NMR spectrum was obtained for sample K070715 at a spinning rate of 30 kHz (Fig. 10b). The estimated abundance for Al^{IV} in the bulk sample K070715 from the peak volume was about 1.6%. The actual abundance in topaz-OH I of the sample must be less, as is also clear from Figure 11.

^{1}H-^{27}Al CP-MAS NMR spectra were also obtained at a spinning rate of 20 kHz for all samples (not shown). The spectra in general resemble the respective ^{27}Al MAS NMR spectra, suggesting the peaks are (dominantly) from hydrous (topaz-OH) phase(s). Nevertheless, small differences in peak shapes from those of the corresponding MAS spectra and small variations with experimental parameters (e.g., position of the transmitter for the ^{27}Al channel) are sometimes observed, in part due to limited frequency range of excitation as a result of low RF power used during CP.

It is also worth mentioning that the ^{1}H-^{27}Al CP-MAS NMR spectrum reported in Xue et al. (2006) for a sample synthesized at ca. 12 GPa and 1200–1300 °C (F050612) (topaz-OH + kyanite + stishovite) resemble the ^{27}Al MAS and ^{1}H-^{27}Al CP-MAS NMR spectra for topaz-OH I + II samples (K070715 and K080926b) described above. This again supports the conclusion from ^{1}H-^{29}Si CP-MAS NMR that this sample also contained mixed topaz-OH I + II phases.

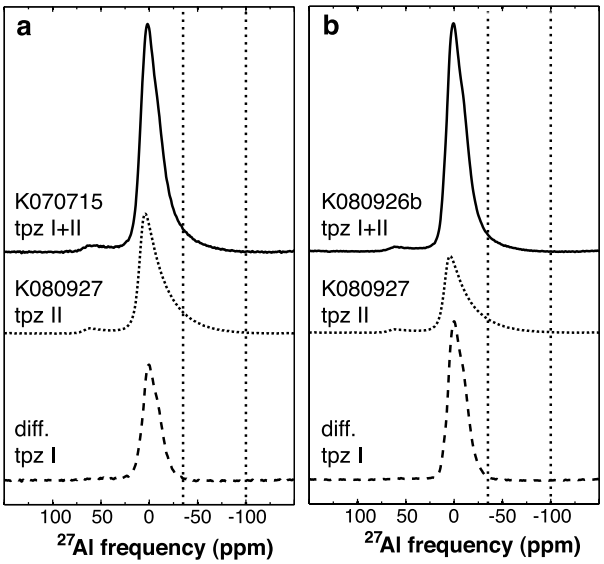

Figure 11. Comparison of ^{27}Al MAS NMR spectrum for samples containing topaz-OH I + II (**a**: K070715; **b**: K080926b) (top, solid line) and that containing only topaz-OH II (K080927) (middle, dotted line), all acquired at a spinning rate of 22 kHz (as shown in Fig. 9), and the difference spectra of the two (bottom, dashed line). The latter were obtained by adjusting the relative intensities of the two spectra so that the sum of squared intensities in the –35 to –100 ppm region (delineated by vertical, dotted lines), where topaz-OH I is not expected, are minimized in the difference spectrum. Further expanding the reference region beyond –35 ppm would yield prominent negative intensity for the difference spectra.

Discussion

^{29}Si chemical shift range for octahedral Si

The ^{29}Si chemical shift of silicates is known to be sensitive to the coordination number of Si. For inorganic silicates, data for tetrahedral Si typically fall within the range of –60 to –120 ppm (Stebbins 1995); limited data for pentacoordinate Si in silicate glasses (Gaudio et al. 2008; Xue et al. 1991) and crystalline calcium silicates (Kanzaki et al. 1991; Stebbins and Poe 1999) give ^{29}Si chemical shifts of –124 to –150 ppm; the reported data for octahedral Si fall in the range of –158 to –221 ppm (Phillips et al. 1997; Stebbins 1995; Xue et al. 2006). For the latter, it has been noted that octahedral Si with one or more edge-sharing $SiO_6/AlO_6/MgO_6$ octahedral next-nearest neighbors (NNN) tend to have less negative ^{29}Si chemical shifts (–158 to –191.3 ppm) than those without such neighbors (–191.7 to –221 ppm) (Kanzaki et al. 1992; Phillips et al. 1997; Xue et al. 2006). Among them, our previous study for phase egg (Xue et al. 2006) revealed three ^{29}Si NMR peaks near –183, –174, and –158 ppm, which were attributed to octahedral Si with 2Si1Al, 1Si2Al, and 3Al edge-sharing octahedral NNN, respectively, showing progressively less negative chemical shift with increasing Al/Si ratio in the edge-sharing NNN sites. The peak near –158 ppm gave the least negative ^{29}Si chemical shift for octahedral Si known by that time. Predominance of ^{29}Si chemical shift by the number of edge-sharing (rather than corner-sharing) NNN is also known for SiS_4 tetrahedra in thiosilicates (though with an opposite trend) (Eckert et al. 1989). The reported ^{29}Si chemical shifts for the corresponding groups in organosilicon compounds are in general similar, but cover somewhat wider and overlapping ranges (SiO_4: –44 to –110 ppm; SiO_5: –102 to –144 ppm; SiO_6: –135 to –197 ppm) (Kemmitt and Milestone 1995; Marsmann 1981; Swamy et al. 1990).

The main ^{29}Si NMR peak near –80 to –83 ppm for topaz-OH I and II are typical of those for tetrahedral Si, and can thus be assigned unambiguously. The broad, continuous distribution of intensities in the region of –190 to –130 ppm observed for topaz-OH II (and II + I) from this study largely overlap with, but

extend further beyond (to higher frequency) the typical chemical shift range for octahedral Si in inorganic silicates, as described above. In particular, the main, narrower component near –178 ppm for topaz-OH II is typical of octahedral Si. As to the highest-frequency extreme (to ca. –130 ppm) of the broader component for topaz-OH II and the weak peak near –133 ppm for topaz-OH I at high *P-T*, if judged purely from chemical shift alone, it would be difficult to exclude the possibility of pentacoordinte Si, because it lies within the reported range (–124 to –150 ppm) for such group in limited inorganic silicates as described above. Nevertheless, several lines of evidence suggest that they are most likely all from octahedral Si.

First, because the intensities for topaz-OH II span continuously from –190 to –130 ppm with the majority within the known range for octahedral Si (but not pentacoordinate Si) (see Fig. 5f), it would be most reasonable if the entire envelope belongs to octahedral Si.

Second, the extreme chemical shift near –130 ppm is in fact fully consistent with the local structures of octahedral Si expected for topaz-OH I and II. As detailed in subsequent sections, octahedral Si in topaz-OH II have local structures resembling those in ideal topaz-OH (octahedra with two edge-sharing octahedral NNN) and diaspore (octahedra with four edge-sharing octahedral NNN), as well as those in between (octahedra with three edge-sharing octahedral NNN). The peak maximum for topaz-OH II near –178 ppm, which lies between peaks of phase egg with 2Al1Si (–174 ppm) and 1Al2Si (–183 ppm) edge-sharing octahedral NNN, most likely results from dominant octahedral Si sites with two edge-sharing AlO_6 octahedra. Provided the trend of increasing number of edge-sharing octahedral NNN favors less negative ^{29}Si chemical shift described above applies, the least negative chemical shift that may be expected for octahedral Si in topaz-OH II would be for those with four edge-sharing AlO_6 neighbors. The latter most likely gives less negative chemical shifts than those with three edge-sharing AlO_6 neighbors (e.g., –158 ppm in phase egg). Therefore, it is not unreasonable to assign the high-frequency extreme of the continuous peak for topaz-OH II near –130 ppm (and the peak near –133 ppm observed for topaz-OH I) to octahedral Si with four edge-sharing AlO_6 neighbors. Such chemical shift values are also consistent with the range observed for SiO_6 groups in organosilicon compounds (–135 to –197 ppm) as described above. In particular, because SiO_6 with multiple edge-sharing AlO_6 neighbors are expected to have small Si-O-Al angles (as compared to those with only corner-sharing neighbors), the assignment is consistent with the observation that the least negative chemical shifts (to –135 ppm) for SiO_6 in organosilicon compounds occur only in small five-membered (-C-O-Si-O-C-) rings that have small Si-O-C angles (Kemmitt and Milestone 1995; Kubicki and Heaney 2003).

Third, as is discussed in Kanzaki (2010) (also see below), topaz-OH I and II, along with diaspore (Hill 1979), share the same basic topology based on hexagonally close-packed array of O atoms with cations occupying (different combinations of) tetrahedral and octahedral interstices (sites). Although the development of pentacoordinate cation sites (e.g., through the creation of oxygen site vacancies) in the topaz-OH or diaspore structure is physically feasible, there is no evidence or compelling need for such a structure model.

Therefore, it may be concluded that the observed peak in the range of –130 to –190 ppm for topaz-OH II and I may be most reasonably attributed to octahedral Si with two to four edge-sharing octahedral NNN, with the most extreme peak near –133 ppm observed for topaz-OH I and the high-frequency extreme of the continuous peak for topaz-OH II attributable to octahedral Si with four edge-sharing AlO_6 neighbors. This thus extends the known chemical shift range for octahedral Si in inorganic silicates to overlap with that of pentacoordinate Si (–124 to –150 ppm), albeit still in good agreement with the known range (–135 to –197 ppm) for SiO_6 in organosilicon compounds. The wide range of chemical shift for octahedral Si in inorganic silicates is in part a result of the variety (different numbers and types) of edge-sharing NNN environments.

Structural features of topaz-OH I

Topaz-OH I under low *P-T* condition (7 GPa, 640 °C). Topaz-OH I synthesized at 7 GPa and 640 °C (K081113) has a composition within uncertainty of that for ideal topaz-OH [$Al_2SiO_4(OH)_2$]. The ^1H-^{29}Si CP-MAS NMR spectra contain a single, narrow peak near –83.4 ppm, typical of tetrahedral Si. The ^{27}Al MAS NMR pattern can be reasonably simulated by a single Al site with a ^{27}Al chemical shift of 8.2 ppm typical of octahedral Al (with some extra intensities that may be due to imperfections in the structure). All these results are consistent with a largely ordered structure of topaz-OH I (consisting of SiO_4 tetrahedra and AlO_6 octahedra, see Fig. 12a) at relatively low *P-T*, as was also reported by previous X-ray (Northrup et al. 1994; Wunder et al. 1993) and neutron diffraction (Chen et al. 2005) studies. The observed relatively small ^1H chemical shift (3.8 ppm) is consistent with the weak hydrogen-bonding (O-H···O distances of 2.9–3.1 Å) revealed from diffraction studies (Chen et al. 2005; Northrup et al. 1994) [see Xue and Kanzaki (2009) for the inverse correlation of the two parameters]. However, although two hydrogen sites were identified in topaz-OH from the latter studies, only a single narrow, symmetric peak is observed in both the ^1H MAS NMR (FWHM = 1.7 ppm at 40 kHz MAS) and 2D ^1H CRAMPS-MAS NMR spectra (FWHM = 0.35 ppm in the scaled CRAMPS dimension). A similar observation has also been reported previously for chondrodite, $Mg_5Si_2O_8(OH)_2$ (with a single ^1H MAS NMR peak at 1.1 ppm for two hydrogen sites) (Phillips et al. 1997). This could be due to insensitivity of ^1H NMR to hydrogen bonding within the weak hydrogen-bonding regime (Xue and Kanzaki 2009).

Topaz-OH I under high *P-T* conditions (13.5–14 GPa, 1300–1500 °C). Topaz-OH I in samples synthesized at higher *P-T* in the vicinity of the polymorphic phase transition boundary (13.5–14 GPa, 1300–1500 °C, K070715 and K080926b) show compositions with consistently lower Si/Al ratios (0.43–0.45) than that of the ideal composition. Although both samples contain some coexisting topaz-OH II, from the preceding analysis (spectral subtraction), it may be concluded that topaz-OH I in both samples contain a small fraction of octahedral Si (~3%) with a unique chemical shift around –133 ppm, and could also contain a smaller fraction of tetrahedral Al (<1.6%).

A simple, intuitive scenario for the lower (than ideal) Si/Al ratios is that excess Al enters Si (tetrahedral) sites, while the basic structure of ideal topaz-OH I is retained. If the observed

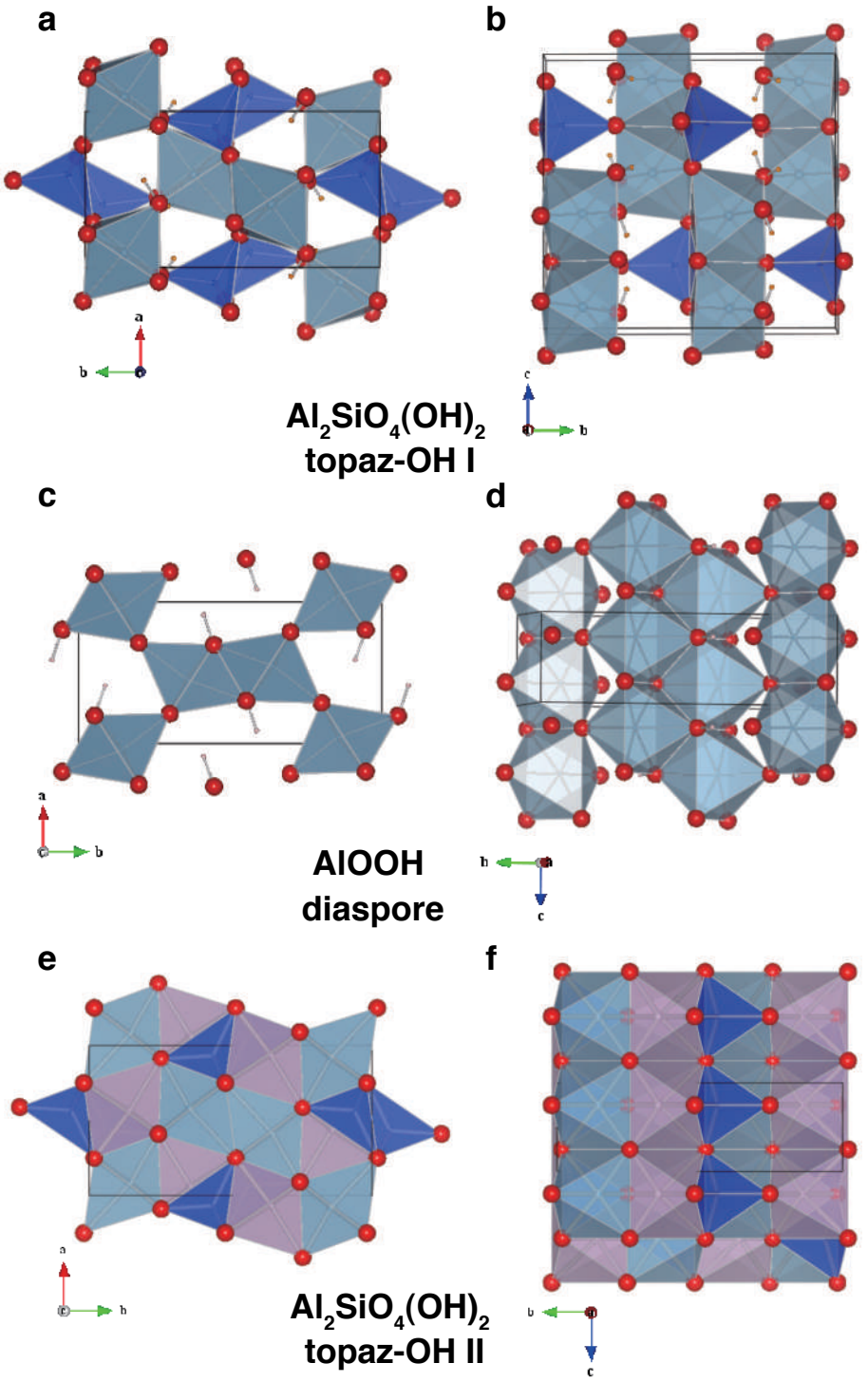

FIGURE 12. Comparison of the crystal structures of ideal topaz-OH I (Northrup et al. 1994) (**a**, **b**), diaspore (Hill 1979) (**c**, **d**), and topaz-OH II (Kanzaki 2010) (**e**, **f**). For **a**–**d**, light-colored octahedra stand for AlO_6 and dark-colored tetrahedra stand for SiO_4; for **e**–**f**, the notation is similar, except that there are two types of octahedral sites [Oc1: light-colored (gray for the color version), Oc2: dark-colored (purple for the color version)], and all tetrahedral and octahedral sites are only partially occupied (by Al+Si). Large spheres represent O atoms, and small spheres represent H atoms for all. Boxes delineate the unit-cell dimensions. Drawings have been produced with VESTA (Momma and Izumi 2008). Color online.

small fraction of octahedral Si is ignored, the observed non-ideal composition would requires 3.3–4% of Al entering tetrahedral sites. If a small fraction of Si-Al exchange occurs between the octahedral and tetrahedral sites (as indicated by the presence of ca. 3% octahedral Si), the tetrahedral Al required would be somewhat higher (5%). The observed NMR spectra seem to suggest significantly lower concentration of tetrahedral Al (<1.6%). Furthermore, this model would imply that all octahedral sites have two edge-sharing octahedral neighbors (as in the ideal topaz-OH structure). It would then be difficult to explain the observed extreme chemical shift (–133 ppm) for octahedral Si, which most likely have four edge-sharing AlO_6 neighbors (see above).

A more plausible scenario for the lower Si/Al ratios can be envisioned from the greater (than ideal) occupied octahedral/tetrahedral site ratio (>2.2) derived from the estimated abundances of Si^{VI}, Si^{IV}, Al^{VI}, and Al^{IV} and the measured Si/Al ratio (see Table 3). The latter may be achieved through occupancy of normally vacant octahedral sites and concurrent creation of vacancies in the tetrahedral sites. The (Al-excess) composition may be regarded as solid solution between $Al_2SiO_4(OH)_2$ (ideal topaz-OH) and AlOOH (diaspore) (i.e., Al+H substitution for Si). As further shown for topaz-OH II below (also see Figs. 12e–12f), there are two types of normally vacant octahedral sites (interstices in the hexagonally close-packed oxygen array) in topaz-OH; one is above or below the regular octahedral sites along the *c* axis (Oc1 in Fig. 13), another is laterally displaced from the chains of regular octahedra (Oc2 in Fig. 13). The former (Oc1) resembles those in diaspore. As a matter of fact, there are considerable structural similarities between topaz-OH I and diaspore (see Figs. 12a–12d). Both have the same space group *Pbnm* with unit-cell parameters of a = 4.7203(8), b = 8.9207(15), c = 8.4189(15) Å for topaz-OH I (Northrup et al. 1994), and a = 4.4007(6), b = 9.4253(13), c = 2.8452(3) Å (Hill 1979) for diaspore. The a and b lengths of diaspore are similar to those of topaz-OH, whereas its c length is about 1/3 of the latter (corresponding to the length of one octahedron). In terms of polyhedral connec-

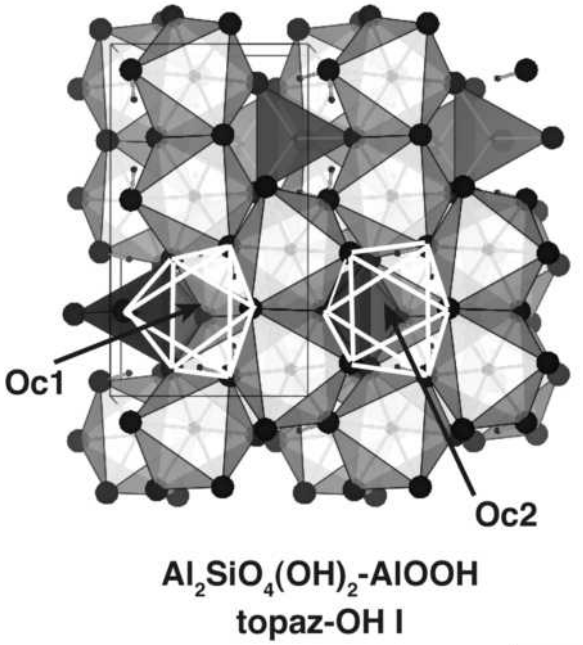

FIGURE 13. The crystal structure of topaz-OH I with possible positions of occupied, normally vacant octahedral sites outlined (Oc1 and Oc2 as labeled). The notations are the same as Figures 12a–12b. Drawings have been produced with VESTA (Momma and Izumi 2008). Color online.

tivity, the diaspore structure consists of infinite edge-sharing double octahedral chains that are elongated along the *c* axis and interconnected to neighboring chains by corner-sharing, form (2 × 1) octahedron-sized channels in between (Figs. 12c–12d); the ideal topaz-OH I structure contains chains with a repeating unit of two AlO_6 octahedra and one SiO_4 tetrahedron (Fig. 12a). If all the tetrahedral sites in ideal topaz-OH I become vacant, and all neighboring vacant (diaspore-type) octahedral sites (i.e., those above and below regular octahedral sites along the *c* axis) are occupied instead, the diaspore structure would be obtained. Therefore, the excess Al of topaz-OH I produced at elevated *P-T* conditions may be well accounted for by partial occupancy of normally vacant, diaspore-type octahedral sites (Oc1 in Fig. 13) and concurrent creation of vacancies in adjacent (face-sharing) tetrahedral sites. The observation of octahedral Si suggests that some of the Si atoms also move from tetrahedral to octahedral site(s) (which may or may not be the result of simple Si-Al exchange between tetrahedral and octahedral sites). If a Si atom is moved from a tetrahedral site to a neighboring Oc1 site, the latter would have four edge-sharing octahedral neighbors. This would be consistent with the observed ^{29}Si chemical shift (near –133 ppm), because the largest population of octahedral Si is expected to have four AlO_6 edge-sharing neighbors due to the predominance of Al in octahedral sites. It should be noted that Oc2 sites (shown in Fig. 13) similarly may have four edge-sharing octahedral neighbors [if located next to a (face-sharing) tetrahedral site], and thus cannot be excluded. The predominance of octahedral Si with four edge-sharing AlO_6 neighbors in topaz-OH I (giving a ^{29}Si peak near –133 ppm), rather than regular octahedral sites with two edge-sharing octahedral neighbors (^{29}Si peak near –178 ppm) may be explained by oxygen bond valence. If Si enters a regular octahedral site, each SiO_6 would be linked to four (corner-sharing) SiO_4 tetrahedra and two edge-sharing AlO_6 octahedra. Four of the six O atoms in the SiO_6 octahedron would be coordinated to one Si^{VI}, one Al^{VI}, and one Si^{IV}, and thus would be significantly over-bonded. If Si enters Oc1 or Oc2 sites as shown in Figure 13 (while leaving a neighboring tetrahedral site vacant), each SiO_6 would have four edge-sharing AlO_6 neighbors, but only one SiO_4 neighbor (at most), and thus would lead to less over-bonded O atoms. The proportions of octahedral cations (Si+Al) occupying normally vacant sites are estimated to be >3–4% for the two samples from the analyzed Si/Al ratio and the estimated abundances of Si^{VI}, Si^{IV}, Al^{VI}, and Al^{IV} (assuming the creation of each tetrahedral vacancy is accompanied by occupancy of one nominally vacant octahedral site). It should be noted that because Oc1 (diaspore-type, vacant octahedral) sites and (at least) part of the Oc2 sites have four edge-sharing octahedral NNN, the proportion of Al sites affected by such defects would be significantly higher. The lack of well-defined quadrupolar pattern for the ^{27}Al MAS NMR spectra of topaz-OH I synthesized under high *P-T* conditions may thus be accounted for.

In brief, topaz-OH I produced under high *P-T* (in the vicinity of the polymorphic phase transition boundary) have lower-than-ideal Si/Al ratios that may be described as solid solution between $Al_2SiO_4(OH)_2$ (for ideal topaz-OH) and AlOOH (diaspore). The nonstoichiometric composition may be largely accounted for by the occupancy of normally vacant octahedral sites by excess Al and concurrent creation of vacancies in the tetrahedral sites of the ideal topaz-OH I structure. A small fraction (ca. 3%) of Si in octahedral coordination are also observed, and seem to preferentially enter normally vacant octahedral sites (with four edge-sharing octahedral NNN). The development of these defect structures would increase the configurational entropy of topaz-OH, and is thus favored at high temperature.

Structural features of topaz-OH II

Topaz-OH II synthesized at 13.5–14 GPa, 1300–1500 °C (K070715, K071126, and K080927), like topaz-OH I obtained at similar *P-T* (in the vicinity of the phase transition boundary), show compositions with consistently lower Si/Al ratios (0.41–0.46) than that of the ideal topaz-OH composition, which may again be described as solid solution between $Al_2SiO_4(OH)_2$ and AlOOH.

The ^{1}H NMR spectra of topaz-OH II (K071126 and K080927) suggest significant proton disorder, with a distribution of (and overall greater) chemical shifts than topaz-OH I, which would correspond to a distribution of (and overall shorter) hydrogen-bonding distances from the known inverse correlation of the two parameters (Xue and Kanzaki 2009). ^{29}Si MAS NMR spectra suggest greater local disorder around tetrahedral Si and also the presence of significant abundance (33–37%) of Si in octahedral coordination. The proportion of Al in tetrahedral coordination derived from ^{27}Al 3Q MAS NMR (2–3%) is, in comparison, much less abundant. From the estimated abundances of Si^{VI}, Si^{IV}, Al^{VI}, and Al^{IV} and the measured Si/Al ratio, the occupied octahedral/tetrahedral ratio (for Si+Al) is inferred to be 3.6 for both topaz-OH II samples, which is significantly higher than that (2) of ideal topaz-OH I (see Table 4).

TABLE 4. Si and Al site distribution in topaz-OH I and II based on electron microprobe analysis (EPMA) and NMR results

Phase†	^{29}Si MAS NMR		^{27}Al 3Q MAS NMR		EPMA		Site fraction among all cations (Si+Al)‡						ΣO/ΣT	Si^{VI}/ΣO	Al^{IV}/ΣT	vacant T/ΣT§
	Si^{IV}/ΣSi	Si^{VI}/ΣSi	Al^{IV}/ΣAl	Al^{VI}/ΣAl	Si/Al	Si/(Si+Al)	Si^{IV}/Σ (Si+Al)	Si^{VI}/Σ (Si+Al)	Al^{IV}/Σ (Si+Al)	Al^{VI}/Σ (Si+Al)	ΣT/Σ (Si+Al)	ΣO/Σ (Si+Al)				
Tpz I, ideal	1	0	0	1	0.5	0.333	0.333	0.000	0.000	0.667	0.333	0.667	2.00	0.000	0.00	0.00
Tpz I, K070715*	0.973	0.027	0.016	0.984	0.44	0.306	0.297	0.008	0.011	0.683	0.308	0.692	2.24	0.012	0.04	0.07
Tpz I, K080926b*	0.972	0.028	0.016	0.984	0.45	0.310	0.302	0.009	0.011	0.679	0.313	0.687	2.20	0.013	0.04	0.06
Tpz II, K071126	0.63	0.37	0.022	0.978	0.46	0.315	0.198	0.117	0.015	0.670	0.214	0.786	3.68	0.148	0.07	0.36
Tpz II, K080927	0.67	0.33	0.032	0.968	0.41	0.291	0.195	0.096	0.023	0.687	0.218	0.782	3.60	0.123	0.10	0.35

* The Al^{IV}/ΣAl ratio for the bulk K070715 is used for a rough approximation (upper limit).
† Tpz I = topaz-OH I; Tpz II = topaz-OH II.
‡ T = tetrahedral Si+Al; O = octahedral Si+Al.
§ Fraction among all available T sites (in the ideal topaz-OH I structure) that are vacant, estimated from ΣO/ΣT assuming the deviation from 2 (for ideal topaz-OH I) results from cations moving from T to O sites.

As described in Kanzaki (2010) and also shown in Figure 12e–12f, the structure of topaz-OH II, derived from Rietveld refinement of powder XRD data for sample K071126 obtained using synchrotron radiation at SPring-8, bears some resemblance to that of the ideal topaz-OH (I) and diaspore structures, all with a space group *Pbnm*. The lattice constants of topaz II are a = 4.72318(5), b = 8.91480(9), and c = 2.77276(3) Å. All three parameters are close to those of diaspore; as for the latter, the a and b lengths are similar to those of topaz-OH I, and the c length is about 1/3 of topaz-OH I (i.e., approximately the length of one octahedron). The latter feature can only be accounted for, given the observed composition, if there is an absence of long-range order in the distribution of cations (Si, Al) in the tetrahedral and octahedral sites along the c-axis. The refined crystal structure contains one tetrahedral site (T, resembling that of topaz-OH I) and two types of octahedral sites, Oc1 (that resemble those of topaz-OH I and diaspore) and Oc2 (that are displaced laterally from the Oc1 chains and located in the (2 × 1) channels of the ideal topaz-OH I structure) (see Fig. 12 for a comparison). All three sites form infinite chains along the c axis, but are only partially occupied (with estimated occupancy of 0.213, 0.705, and 0.082 for T, Oc1, and Oc2, respectively; note the occupancy is relative to all sites in the infinite chain, so that the corresponding occupancy for ideal topaz-OH I would be 0.333, 0.667, and 0, respectively). Although there is no long-range order as revealed by the lattice parameters, local order must be present to prevent face-sharing neighbors of T-Oc1, T-Oc2, and Oc1-Oc2 sites (at least when occupied by Si). Random and partial occupancy of cations (Al, Si) in both Oc1 and Oc2 sites would create octahedral sites with a range of edge-sharing octahedral NNN, from two (as in ideal topaz-OH I), to three, and to four (as in diaspore).

Some insights into the distribution of Si within the octahedral and tetrahedral sites may be gained from the NMR peak shape for Si^{VI}. There is a narrower main component with a maximum near –178 ppm and a broader component extending to about –130 ppm. As discussed above, the main, narrower component near –178 ppm most likely results from octahedral Si with two edge-sharing AlO_6 neighbors. Such a local structure is typical of octahedral sites in the ideal topaz-OH I structure. On the other end, the extreme chemical shift near –130 ppm must result from octahedral Si with four edge-sharing AlO_6 neighbors, which resembles octahedral sites in the diaspore structure. The intensities in the intermediate frequency region most likely result from octahedral Si with a range (2, 3, and 4) of edge-sharing octahedral NNN and different Si/Al ratios in the NNN. The dominance of octahedral Si with two edge-sharing octahedral NNN in topaz-OH II, but not in topaz-OH I with similar compositions may be related to the significantly greater fraction of vacancies in the tetrahedral sites in the former, because octahedral Si would then have less tetrahedral Si NNN and thus more freedom to enter octahedral sites with different numbers of edge-sharing octahedral NNN without leading to significant oxygen overbonding. Unfortunately, similar information (NNN environments) for Al cannot be extracted from the ^{27}Al NMR spectra, because of complications due to quadrupolar coupling and lack of knowledge (and resolution) concerning the NNN effects on its NMR parameters.

Although the refined structure from X-ray diffraction revealed the occupancy of two types of octahedral sites in topaz-OH II, it is difficult to distinguish them by NMR because both would result in octahedral sites with different numbers of edge-sharing octahedral NNN and contribute to the range of ^{29}Si NMR intensities within –190 to –130 ppm.

The ^{1}H NMR results are also consistent with the structure described above. In the ideal topaz-OH I structure, protons are bonded to two corner-sharing octahedral Al with relatively weak hydrogen-bonding (O-H···O distances of 2.9–3.1 Å) and accordingly produce a relatively low ^{1}H chemical shift (3.8 ppm). On the other hand, protons in AlOOH diaspore are bonded to three edge-sharing AlO_6 octahedra (because of the continuous edge-sharing double octahedral chain) with stronger hydrogen bonding (O-H···O distances of 2.65 Å) and accordingly result in larger ^{1}H chemical shift (9.4 ppm). The stronger hydrogen bonding of the latter may be attributed to greater bond valence when an oxygen atom is bonded to three rather than two Al, which would in turn favors stronger hydrogen bonding for the proton attached to it. In the structure of topaz-OH II, because of the significantly greater proportion of occupied octahedral sites (than ideal topaz-OH I structure), a significant proportion of the protons must be bonded to three edge-sharing octahedra (SiO_6 and/or AlO_6); the varying and overall larger oxygen bond valence (due to different number and types (Si, Al) of bonded octahedral cations) would result in a range of (and overall shorter) hydrogen bonding distances, and accordingly a range of (and overall larger) ^{1}H chemical shifts (extending to about 12 ppm). The narrower component near the peak maximum (4.8–4.9 ppm) likely represents OH shared by two edge-sharing octahedra.

Characteristics of the polymorphic phase transition of topaz-OH

The (equilibrium) composition of topaz-OH I produced from a (nominal) $Al_2SiO_4(OH)_2$ (and more Si-rich $AlSiO_3OH$) start-

ing composition appears to change from nearly stoichiometric at lower *P-T* to more Al-rich compositions [describable by $Al_2SiO_4(OH)_2$-AlOOH solid solution, or Al+H for Si substitution] at higher *P-T* in the vicinity of the polymorphic phase transition boundary. The compositional change is most likely accompanied by the development of relatively isolated defects (vacancies in tetrahedral sites and Si/Al in adjacent normally vacant octahedral sites) in an otherwise ordered topaz-OH structure at higher *P-T*. This leads to a somewhat greater occupied octahedral/tetrahedral site ratio (than the ideal structure). These compositional and structural changes would be consistent with greater entropy at higher temperatures. Composition variation and nonstoichiometry at elevated temperatures have been widely observed for many inorganic compounds (e.g., $MgAlO_4$ spinel in the MgO-Al_2O_3 system), and are often accompanied by equilibrium population of intrinsic structural defects (Tilley 2008).

The polymorphic phase transition of topaz-OH I and II appears to be isochemical, with both phases near the transition boundary having more Al-rich compositions than the ideal topaz-OH. The most prominent structural changes accompanying the phase transition include significantly greater occupied octahedral sites (especially greater octahedral Si) and correspondingly less occupied tetrahedral sites, and significantly greater disorder in cation distribution among all (partially occupied) sites (to the extent that long-range order along the *c* axis is lost) in topaz-OH II. These structural changes would be accompanied by an abrupt increase in density and configurational entropy, and are thus favored with increasing *P-T*. Exchange of Si-Al between tetrahedral and octahedral sites, although also observed, is less significant, in comparison. This type of polymorphic phase transition, as far as the authors are concerned, has not been observed in any other phases, and thus is unique from a crystal-chemical point of view.

Acknowledgments

We thank Simon Kohn, an anonymous reviewer, and the associate editor (Bjorn Mysen) for constructive comments. We are also grateful to Eiji Ito for collaboration with sample synthesis during the early stage of the study, to Takuya Matsuzaki for assistance with electron microprobe analysis, and to Ken-ichi Funakoshi for access to the multi-anvil press at SPring-8. This study was supported by Grants-in-Aid for Scientific Research funded by the Ministry of Education, Culture, Sports, Science and Technology of Japan.

References cited

Amoureux, J.-P. and Fernandez, C. (1998) Triple, quintuple and higher order multiple quantum MAS NMR of quadrupolar nuclei. Solid State Nuclear Magnetic Resonance, 10, 211–223.

Amoureux, J.-P., Fernandez, C., and Frydman, L. (1996a) Optimized multiple-quantum magic-angle spinning NMR experiments on half-integer quadrupoles. Chemical Physics Letters, 259, 347–355.

Amoureux, J.-P., Fernandez, C., and Steuernagel, S. (1996b) Z filtering in MQMAS NMR. Journal of Magnetic Resonance A, 123, 116–118.

Bennett, A.E., Rienstra, C.M., Auger, M., Lakshmi, K.V., and Griffin, R.G. (1995) Heteronuclear decoupling in rotating solids. Journal of Chemical Physics, 103, 6951–6958.

Bielecki, A., Kolbert, A.C., and Levitt, M.H. (1989) Frequency-switched pulse sequences: Homonuclear decoupling and dilute spin NMR in solids. Chemical Physics Letters, 155, 341–346.

Chen, J.R., Lager, G.A., Kunz, M., Hansen, T.C., and Ulmer, P. (2005) A Rietveld refinement using neutron powder diffraction data of a fully deuterated topaz, $Al_2SiO_4(OD)_2$. Acta Crystallographica Section E-Structure Reports Online, 61, I253–I255.

Churakov, S.V. and Wunder, B. (2004) Ab-initio calculations of the proton location in topaz-OH, $Al_2SiO_4(OH)_2$. Physics and Chemistry of Minerals, 31, 131–141.

Cory, D.G. and Ritchey, W.M. (1988) Suppression of signals from the probe in Bloch decay spectra. Journal of Magnetic Resonance, 80, 128–132.

Eckert, H., Kennedy, J.H., Pradel, A., and Ribes, M. (1989) Structural transformation of thiosilicate glasses: ^{29}Si MAS-NMR evidence for edge-sharing in the system Li_2S-SiS_2. Journal of Non-Crystalline Solids, 113, 287–293.

Gaudio, S.J., Sen, S., and Lesher, C.E. (2008) Pressure-induced structural changes and densification of vitreous $MgSiO_3$. Geochimica et Cosmochimica Acta, 72, 1222–1230.

Hill, R.J. (1979) Crystal structure refinement and electron density distribution in diaspore. Physics and Chemistry of Minerals, 5, 179–200.

Kanzaki, M. (2008) Elastic wave velocities and Raman shift of MORB glass at high pressures—Comment. Journal of Mineralogical and Petrological Sciences, 103, 427–428.

——— (2010) Crystal structure of a new high-pressure polymorph of topaz-OH. American Mineralogist, 95, 1349–1352.

Kanzaki, M., Stebbins, J.F., and Xue, X. (1991) Characterization of quenched high pressure phases in $CaSiO_3$ system by XRD and ^{29}Si NMR. Geophysical Research Letters, 18, 463–466.

——— (1992) Characterization of crystalline and amorphous silicates quenched from high pressure by ^{29}Si MAS NMR spectroscopy. In Y. Syono, and M.H. Manghnani, Eds., High-Pressure Research: Application to Earth and Planetary Sciences, 67, p. 89–100. Terra Scientific Publishing Company, Tokyo.

Kanzaki, M., Xue, X., Fukui, H., and Ito, E. (2006) High-pressure form of topaz-OH: Structure and characterization by NMR and Raman. 9th General Meeting of the International Mineralogical Association (IMA), Kobe, Japan, p. 134–134.

Kemmitt, T. and Milestone, N.B. (1995) The ring size influence on Si-29 NMR—chemical-shifts of some spirocyclic tetracoordinate and pentacoordinate diolato silicates. Australian Journal of Chemistry, 48, 93–102.

Komatsu, K., Kagi, H., Okada, T., Kuribayashi, T., Parise, J.B., and Kudoh, Y. (2005) Pressure dependence of the OH-stretching mode in F-rich natural topaz and topaz-OH. American Mineralogist, 90, 266–270.

Kubicki, J.D. and Heaney, P.J. (2003) Molecular orbital modeling of aqueous organosilicon complexes: Implications for silica biomineralization. Geochimica et Cosmochimica Acta, 67, 4113–4121.

Libowitzky, E. (1999) Correlation of O-H stretching frequencies and O-H···O hydrogen bond lengths in minerals. Monatshefte für Chemie, 130, 1047–1059.

MacKenzie, K.J.D. and Smith, M.E. (2002) Multinuclear Solid-State NMR of Inorganic Materials, 6, p. 727. Pergamon materials series, Elsevier Science, Oxford.

Malfait, W.J. and Xue, X. (2010) The nature of hydroxyl groups in aluminosilicate glasses: quantifying Si-OH and Al-OH abundances along the SiO_2-$NaAlSiO_4$ join by ^{1}H, ^{27}Al-^{1}H and ^{29}Si-^{1}H NMR spectroscopy. Geochimica et Cosmochimica Acta, 74, 719–737.

Marsmann, H. (1981) ^{29}Si-NMR spectroscopic results. In P. Diehl, E. Fluck, and R. Kosfeld, Eds., Oxygen-17 and silicon-29: NMR Basic Principles and Progress, p. 65–235. Springer-Verlag, Berlin.

Momma, K. and Izumi, F. (2008) VESTA: A three-dimensional visualization system for electronic and structural analysis. Journal of Applied Crystallography, 41, 653–658.

Nakamoto, K., Margoshes, M., and Rundle, R.E. (1955) Stretching frequencies as a function of distances in hydrogen bonds. Journal of American Chemical Society, 77, 6480–6486.

Northrup, P.A., Leinenweber, K., and Parise, J.B. (1994) The location of H in the high-pressure synthetic $Al_2SiO_4(OH)_2$ topaz analogue. American Mineralogist, 79, 401–404.

Ono, S. (1999) High temperature stability limit of phase egg, $AlSiO_3(OH)$. Contributions to Mineralogy and Petrology, 137, 83–89.

Pawley, A.R., McMillan, P.F., and Holloway, J.R. (1993) Hydrogen in stishovite, with implications for mantle water content. Science, 261, 1024–1026.

Phillips, B.L., Burnley, P.C., Worminghaus, K., and Navrotsky, A. (1997) ^{29}Si and ^{1}H NMR spectroscopy of high-pressure hydrous magnesium silicates. Physics and Chemistry of Minerals, 24, 179–190.

Schmidt, M.W., Finger, L.W., Angel, R.J., and Dinnebier, R.E. (1998) Synthesis, crystal structure, and phase relations of $AlSiO_3OH$, a high-pressure hydrous phase. American Mineralogist, 83, 881–888.

Stebbins, J.F. (1995) Nuclear magnetic resonance spectroscopy of silicates and oxides in geochemistry and geophysics. In T.J. Ahrens, Ed., Mineral Physics and Crystallography: A handbook of physical constants, p. 303–331. American Geophysical Union, Washington, D.C.

Stebbins, J.F. and Poe, B.T. (1999) Pentacoordinate silicon in high-pressure crystalline and glassy phases of calcium disilicate ($CaSi_2O_5$). Geophysical Research Letters, 26, 2521–2523.

Swamy, K.C.K., Chandrasekhar, V., Harland, J.J., Holmes, J.M., Day, R.O., and Holmes, R.R. (1990) Pentacoordinated molecules. 79. Pentacoordinate acyclic and cyclic anionic oxysilicates. A silicon-29 NMR and X-ray structural study. Journal of the American Chemical Society, 112, 2341–2348.

Tilley, R.J.D. (2008) Defects in Solids, 529 p. Wiley, New York.

Vega, A.J. (1992) CP/MAS of quadrupolar $S = 3/2$ nuclei. Solid State Nuclear Magnetic Resonance, 1, 17–32.

Wunder, B., Rubie, D.C., Ross, C.R.I., Medenbach, O., Seifert, F., and Schreyer, W. (1993) Synthesis, stability and properties and of $Al_2SiO_4(OH)_2$: A fully hydrated analogue of topaz. American Mineralogist, 78, 285–297.

Xue, X.Y. and Kanzaki, M. (2007) High-pressure -$Al(OH)_3$ and -AlOOH phases and isostructural hydroxides/oxyhydroxides: New structural insights from high-resolution ^{1}H and ^{27}Al NMR. Journal of Physical Chemistry B, 111, 13156–13166.

——— (2009) Proton distributions and hydrogen bonding in crystalline and glassy hydrous silicates and related inorganic materials: insights from high-resolution solid-state NMR spectroscopy. Journal of the American Ceramic Society, 92, 2803–2830.

Xue, X.Y., Stebbins, J.F., Kanzaki, M., McMillan, P.F., and Poe, B. (1991) Pressure-induced silicon coordination and tetrahedral structural changes in alkali oxide-silica melts up to 12 GPa: NMR, Raman, and infrared spectroscopy. American Mineralogist, 76, 8–26.

Xue, X.Y., Kanzaki, M., Fukui, H., Ito, E., and Hashimoto, T. (2006) Cation order and hydrogen bonding of high-pressure phases in the Al_2O_3-SiO_2-H_2O system: An NMR and Raman study. American Mineralogist, 91, 850–861.

Xue, X.Y., Kanzaki, M., and Shatskiy, A. (2008) Dense hydrous magnesium silicates, phase D, and superhydrous B: New structural constraints from one- and two-dimensional ^{29}Si and ^{1}H NMR. American Mineralogist, 93, 1099–1111.

Manuscript received December 6, 2009
Manuscript accepted April 25, 2010
Manuscript handled by Bjorn Mysen